Soft Matter

PAPER

View Article Online
View Journal | View Issue

Cite this: *Soft Matter*, 2025, **21**, 4517

Cholesteric liquid crystal roughness models: from statistical characterization to inverse engineering†

Ziheng Wang, Phillip Servio and Alejandro D. Rey *

The surface geometry, particularly the curvature and roughness, play crucial roles in the functionalities of bio-compatible cholesteric liquid crystal (CLC) substrates. For example, experiments show increased alignment of hBMSCs (human bone-marrow-derived stromal cells) with larger curvature on a cylindrical manifold [Callens *et al.*, *Biomaterials*, 2020, **232**, 119739]. Previous studies on cholesteric liquid crystal surfaces have primarily focused on an elastic approach, which does not fully capture the anisotropic nature and multiscale wrinkling profiles. The objective of this research is to characterize the surface geometry of CLCs based on a generalized anisotropic anchoring model (the Rapini–Papoular model). In this paper, we propose both analytic approximations and direct numerical solutions for surface wrinkling, curvature profiles, and surface roughness characterization. We also explore the important limits of the Rapini–Papoular model, including lower bounds for the kurtosis and Willmore energy. The inverse problem offers an alternative approach to measuring the anchoring coefficients, which are difficult to determine experimentally. These findings suggest that surface anchoring is the key determinant of multiscale surface wrinkling patterns. This paper sheds light on the applications and functionalities of surface wrinkling patterns in liquid crystals and their solid analogues. Furthermore, this research incorporates a novel coordinate-free differential geometric approach and provides a general framework for studying dynamic properties and surface evolution.

Received 4th February 2025,
Accepted 10th May 2025

DOI: 10.1039/d5sm00121h

rsc.li/soft-matter-journal

1 Introduction

Synthetic and biological liquid crystals (LCs) are partially ordered materials formed by anisotropic components such as rod-like molecules, fibrils, and filaments which exhibit anisotropic viscoelastic properties.[1–3] Being partially ordered in terms of position and orientation, LCs exhibit both solid (such as anisotropy) and liquid (such as fluidity) characteristics. The macroscopic orientation is denoted by a unit vector or director $\mathbf{n}(x)$ of cholesteric liquid crystals (CLCs) show chirality, which is characterized by the helix pitch P_0, that satisfies $\mathbf{n}(x + P_0) = \mathbf{n}(x)$, that is, the spatial distance for a 2π rotation of the director field is P_0.[4–6] The chiral architecture is ubiquitous in biological materials,[7–11] and was systematically studied by Bouligand. Synthetic and biological cholesteric liquid crystal analogues (CLCAs) are solids with the frozen-in structure of CLCs resulting from various solidification processes.[12–17] As mentioned in more detail, below in this paper, we model and study surface roughness in CLCs for potential biomimetic functional surface applications while CLCAs and related nature's surfaces are the source of biological inspiration as well as geometric data for surface roughness.

Some examples of biological CLCAs are the chitin fibres of the shimmering beetles' exoskeleton,[18–20] cellulosics of biological plywoods[19,21,22] and collagens of human compact bones.[19,23,24] Other important examples of CLCs and CLCAs analogues are DNA both *in vivo* and *in vitro*,[10,25] viruses,[26] spider silk,[27,28] fibroblasts and osteoblasts.[29,30]

Fig. 1 summarizes the main objectives, key phenomena and modelling methods used in this paper. The middle schematic of Fig. 1 shows the surface wrinkling of flower petals, where the cellulosics form a Bouligand structure that is a source of inspiration and data for our surface geometry model for cholesteric liquid crystals. The surface morphology of these materials includes creasing, folding, ridges and wrinkling.[31–36] For example, surface creasing can be found in swelling induced hydrogels[37,38] and others.[39–41] In biological membrane systems such as the Golgi apparatus,[42] mitochondrion membranes[43,44] and cortical tissues,[45–47] surface folding and curvature distribution are key factors affecting biochemical functionalities.[48] In this paper, we study the multiscale wrinkling profile driven by CLC surface anchoring. The two unique characteristics of multiscale CLC surface are: (1) the helix pitch P_0 is in the scale of few micrometers, while the surface wrinkling is in the scale of nanometres.[22,49–52] (2) The surface profile is periodic and tends to form egg-carton

Department of Chemical Engineering, McGill University, 3610 University Street, Montréal, Québec H3A 2B2, Canada. E-mail: alejandro.rey@mcgill.ca

† Electronic supplementary information (ESI) available. See DOI: https://doi.org/10.1039/d5sm00121h

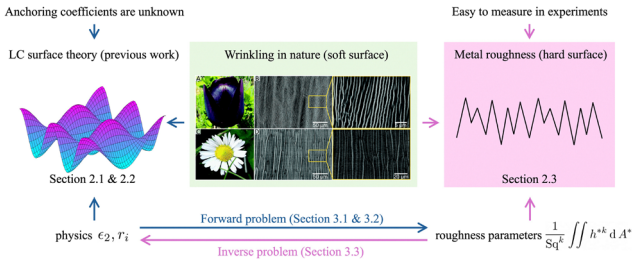

Fig. 1 Graphical summary of the goals, key phenomena and modelling methods of this paper. The blue arrows connect theoretical development of CLC surfaces (physics), and pink arrows connect surface roughness development (experimental data). Centre schematic: this paper is motivated by bio-inspired multiscale wrinkling patterns observed in nature, as in flower petals. Left schematic: we develop a generalized cholesteric liquid crystal shape equation to predict surface roughness and wrinkling as in nature (left upper arrow). We briefly summarize our previous work in Sections 2.1 and 2.2. In these sections, the anisotropic material surface properties of interest are the anchoring coefficients. Right schematic: in this paper we generalize the traditional study and characterization of metal surfaces roughness as inspired by nature (right middle arrow) to describe LCs, considering that CLC surfaces are soft. The quantities of interest in this section are roughness parameters. We study the forward (prediction) problem in Sections 3.1 and 3.2. In the forward problem, we apply the method we developed in previous literature[22,49,50,53–55,59–63] to study the surface roughness. In Section 3.3, we study the inverse problem by solving the physics from measured biological surface roughness parameters. The middle figure is reproduced from ref. 69 with permission from Royal Society of Chemistry (2017).

patterns.[52–56] The two observations imply that the cause of the periodic nanowrinkling profile is not driven by elasticity, since an elastic model does not result in multiscale wrinkling patterns,[57,58] and it cannot explain the P_0-dependent periodicity. To answer those questions, we developed a theoretical framework, shown in Fig. 1 on the left column. Our previous works explain and validate that surface anchoring is the cause of CLC multiscale wrinkling patterns.[22,49,50,53–55,59–63] Cheong *et al.* applied Cahn–Hoffman capillary vector approach to study LC fibre instability,[64–68] which is further generalized and combined with an elastic model to study the elastic CLC membrane wrinkling.[22,49,50] Wang *et al.* studied the 3D structure of the Bouligand structure and successfully obtained egg-carton surfaces.[53–55] These previous works we based on low order contributions to the anchoring energies, while the effect of higher order contributions to anisotropic surface energy is the key focus of this paper.

The right schematic of Fig. 1 shows the domain of surface roughness (or smoothness) for hard material surfaces such as metallic. The surface roughness of hard surface plays an important role in engineering and manufacturing. For example, surface roughness is widely studied to investigate its influence in fluid mechanics,[70–72] electrical properties,[73,74] optical properties,[75,76] wettability,[77,78] friction and adhesion,[79,80] heat distribution,[81] interfacial corrosion,[82,83] and physiochemical process.[84,85] However, similar theoretical and/or experimental studies in soft surfaces are not well established, despite the fact that soft surface roughness are critical to its multifunctionality. For example, the roughness of an endoplasmic reticulum determines different tasks in biology. A smooth endoplasmic reticulum synthesizes lipids and phospholipids,[86,87] while a rough endoplasmic reticulum is a factory for secreted proteins.[88,89] Traditional approaches to studying hard surface roughness rely on statistics, because the hard surfaces are in general non-analytic and we cannot take mathematical derivatives on the surface. The most useful surface roughness tools include parametric methods and functional methods. Parametric methods calculate higher-order moments of the surface profile, where the second-order (root mean square, Sq), third-order (skewness, Rsk) and fourth-order (kurtosis, Rku) moments measure the deviation, asymmetry, and tailedness of surface profile distribution, respectively. Functional methods include autocorrelation function and power spectral density, which are important features of a periodic surface.[84] In this paper, besides adapting traditional approaches from hard surface roughness methods, we also propose a new curvature-based method to support the surface roughness theory for anisotropic soft matter. An advantage of soft surface is that the curvature can be an indicator for surface roughness. We demonstrate that the curvature-based method is equivalent to the membrane geometric energy (such as Willmore energy,[90–92] Helfrich energy[93–95]) and has been widely studied in the theory of geometric flows.[96,97] Other methods such as fractal methods can be used to study the self-similar structure in a nested network, with the advantage of analyzing scale-independent hierarchical structures.[98–100]

In partial summary, the left schematic of Fig. 1 summarizes the physics, theory and computational platform for CLC surfaces, while the right column demonstrates the surface roughness characterization methods widely used for hard surfaces that, as we show here, can be tailored to soft surfaces such as those CLCs. In Sections 3.1 and 3.2 of this paper, we discuss the forward engineering problem by applying the LC surface theory and shape equations we developed in previous papers,[22,55,101] to predict and characterize the surface roughness of LC surfaces. In Section 3.3, we study the inverse surface roughness problem, by using the data from biological surface roughness to reconstruct the LC surface physics (determination of anchoring coefficients).

This inverse problem (Section 3.3) is of great significance to LC material property characterization, because the data of surface roughness is usually much easier to obtain than actual LC anchoring coefficients. For example, methods of measuring surface profile are usually direct methods. Traditional methods include mechanical stylus method,[102] light sectioning method,[103] scattering method,[104,105] scanning electron microscopy,[106,107] scanning probe microscopy,[108,109] machine vision method such as Fourier transform[110] or wavelet transform[111] *etc.* The measurement of anchoring coefficient μ_2, however, is through indirect method which involves calculating a deviation orientation angle.[112,113] Most experimental approaches require the evaluation of a certain twist or deviation angle ϕ, or even higher-order derivatives of ϕ. For example, μ_2 can be calculated by measuring the threshold voltage of Fréedericksz transition V_{th}, the Franck constants K_i (i = 1, 2, 3, 24), and the dielectric susceptibility anisotropy $\Delta\chi$ such that $\mu_2 = \frac{1}{\phi}\frac{\mathrm{d}}{\mathrm{d}x}f(V_{\text{th}}, K_i, \Delta\chi)$. μ_2 can also be evaluated with a rubbed nano-sized groove surface such that $\mu_2 = f(\phi, K_i)$,[114] or with a spectroscopic ellipsometry approach by

solving a PDE dependent on μ_2, ϕ, $\frac{d\phi}{dx}$ and $\frac{d^2\phi}{dx^2}$.[115] The calculation of the deviation angle ϕ is usually hypersensitive to noise since it is based on derivatives. On the other hand, the measurement of surface roughness parameters involves taking integrals and is therefore less affected by noise. For example, if the measured surface is disturbed by δW, where W is the noise following a standard normal distribution $(W \sim \mathcal{N}(0,1))$ and δ is a small amplitude. We can show that the expected value of the root mean square deviates from the model by $\mathbb{E}[\mathrm{Sq}_{\mathrm{measurement}}] - \mathrm{Sq}_{\mathrm{model}} = \delta^2$. It demonstrates that the higher moment methods discussed in this paper are barely affected by the random noise. Another advantage of the new method is that traditional approaches of measuring the anchoring coefficient only give the value of low-order components μ_2 (see Section 2) while the inverse problem engineering can provide the values of higher-order contributions r_i (see Section 3.3) simply by taking higher-order moments.

In summary, the objectives of this paper are as follows:

1. To formulate the generalized governing liquid crystal shape equations that describes the complex surface wrinkling patterns of CLCs, observed in nature;

2. To formulate, execute and validate numerical calculations and generalize high fidelity analytic solutions to the governing nonlinear shape equations that predict multiscale, complex surface roughness in CLCs, as observed in nature;

3. To predict key surface geometry characteristics such as standard (mean, Gaussian) and novel (Casorati, geometric shape index) curvatures and surface roughness statistics (kurtosis, skewness, correlations) of CLCs using biological surface geometry in-put data, including plant leaves and fish skin;

4. To develop and solve the inverse engineering problem in LC surface roughness and use validated results to predict all anchoring coefficients of CLCs that define the surface free energy.

The outline of this paper is as follows. In Section 2.1, we derive the governing shape equation, where the surface profile h is described by a nonlinear partial differential equation. In Section 2.2, we linearize the nonlinear shape equation PDE under a small-wrinkling assumption and solve the PDE with a spectral method. In Section 2.3, we introduce the concepts and definitions of the surface roughness parameters that will be discussed in Section 3; the concepts are summarized in Table 2. The results will be characterized and discussed in Section 3. In Section 3.1, we study the direct numerical solution of the nonlinear shape equation PDE and conclude that small-wrinkling approximation is of high fidelity. In Section 3.2, we study the surface curvatures (Section 3.2.1), higher-order moments (Section 3.2.2), and autocorrelation function (Section 3.2.3), which are obtained from the second derivative, the surface integral, and the self-convolution of the surface profile, respectively. In Section 3.3, we study the inverse engineering problem, and propose an application to find anchoring material properties. The main results, their novelty and significance and the contributions to surface roughness in cholesteric liquid crystals and anisotropic soft matter are presented in the Conclusions. All mathematical details are presented in the ESI.†

The scope of this paper is restricted to an equilibrium cholesteric liquid crystal surface described by an orientation vector or director field. Higher-order tensor models,[116–119] time-dependent phenomena,[120–124] dissipation,[125] dynamics,[126–132] tangential forces and flows,[133–139] and bulk-surface couplings,[101,140] are not included here and are left to future work. Below we use interchangeably biological and nature's surfaces.

2 Methods

In Section 2.1 we introduce the generalized governing shape equation for CLCs that includes higher-order harmonics to the anisotropic surface energy and extends our previously formulated liquid crystal shape equations.[55,59,60] In Section 2.2 we obtain a very useful approximate analytical solution to the generalized nonlinear liquid crystal shape equation to predict surface shapes under small amplitude conditions. The analytical solution is crucial to validate our computational methods and to shed light on shape-generating mechanisms.

2.1 Generalized governing liquid crystal shape equations

The anisotropic surface energy density γ of a cholesteric liquid crystal is the sum of an isotropic surface tension γ_0 and anisotropic contributions. The surface energy density γ is calculated by the generalized Rapini–Papoular model of a polynomial with order $2m$:[53,55,59,60,63]

$$\gamma = \gamma_0 + \sum_{i=1}^{m} \mu_{2i} (\mathbf{n} \cdot \mathbf{k})^{2i} \tag{1}$$

where μ_{2i} (i = 1,…, m) are the anchoring coefficients. $\mathbf{n}$ is the liquid crystal director field, and $\mathbf{k}$ is the surface unit normal. Eqn (1) demonstrates two reflection symmetries: $\mathbf{n} \to -\mathbf{n}$ and $\mathbf{k} \to -\mathbf{k}$. The first symmetry implies that the director $\mathbf{n}$ is indistinguishable from $-\mathbf{n}$, and $\mathbf{n}$ is considered as a line field which forms the real projective plane $\mathbb{R}P^2$. The second symmetry implies that the surface energy density is invariant to different conventions of surface unit normal. However, we pay attention to the direction of $\mathbf{k}$, since $\mathbf{k}$ and $-\mathbf{k}$ alter the sign of curvature definitions. The details concerning this issue have been previously discussed in literature.[62] In our previous work on nanowrinkling of cholesteric surfaces we study cases with m = 1, 2.[22,49,53,55,60] The anchoring coefficients of eqn (1) are restricted by $\gamma > 0$ under all circumstances, and the details are given in Section S2 of ESI.†

The Cahn–Hoffman capillary vector $\boldsymbol{\xi}$ is a useful tool in studying direction-dependent materials since it incorporates interfacial anisotropy into the model.[141–143] The decomposition of Cahn–Hoffman capillary vector $\boldsymbol{\xi}$ results in a tangential component $\boldsymbol{\xi}_\parallel$ and a normal component $\boldsymbol{\xi}_\perp$.[66,144] The details of Cahn–Hoffman capillary vector approach are included in Section S1 of ESI.†

$$\boldsymbol{\xi}(\mathbf{n},\mathbf{k}) = \boldsymbol{\xi}_\perp + \boldsymbol{\xi}_\parallel = \gamma \mathbf{k} + \mathbf{I}_{(\sigma)} \cdot \frac{\partial \gamma}{\partial \mathbf{k}} \tag{2}$$

where $\mathbf{I}_{(\sigma)}$ is the surface unit dyadic: $\mathbf{I}_{(\sigma)} = \mathbf{I} - \mathbf{k}k$. The surface divergence of the capillary vector is the negative value of the

total capillary pressure $p_c = -\nabla_{(\sigma)}\cdot\boldsymbol{\xi}$; $\nabla_{(\sigma)} = \mathbf{I}_{(\sigma)}\cdot\nabla$. The expansion of the surface divergence of $\boldsymbol{\xi}$ contains three capillary pressures:

$$-\nabla_{(\sigma)}\cdot\boldsymbol{\xi} = \underbrace{-\frac{\partial\boldsymbol{\xi}_{\perp}}{\partial\mathbf{k}}:\left(\nabla_{(\sigma)}\mathbf{k}\right)^{\mathrm{T}}}_{\text{Dilation pressure}} \underbrace{-\frac{\partial\boldsymbol{\xi}_{\parallel}}{\partial\mathbf{n}}:\left(\nabla_{(\sigma)}\mathbf{n}\right)^{\mathrm{T}}}_{\text{Director pressure}} \underbrace{-\frac{\partial\boldsymbol{\xi}_{\parallel}}{\partial\mathbf{k}}:\left(\nabla_{(\sigma)}\mathbf{k}\right)^{\mathrm{T}}}_{\text{Rotation pressure}} \quad (3)$$

The three principal capillary pressures in eqn (3) explains the mechanism of anchoring-driven surface wrinkling phenomenon.[22,49,50,64,67] A point p at its neighbourhood $\mathscr{D}_p$ demonstrates three non-vanishing effects: an area dilation of $\mathscr{D}_p$ (dilation pressure), a director $\mathbf{n}$ effect (director pressure) and a $\mathbf{k}$-rotation (rotation pressure) effect. The expansions of principal capillary pressures in the generalized Rapini-Rapoular model are (mathematical details are given in Section S1 of ESI†)

$$\text{Dilation pressure} = 2H\gamma \quad (4)$$

$$\text{Director pressure} = -\sum_{j=1}^{m} 2j\mu_{2j}(\mathbf{n}\cdot\mathbf{k})^{2j-2} \times\left((2j-1)\mathbf{kn}:\nabla_{(\sigma)}\mathbf{n} + (\mathbf{n}\cdot\mathbf{k})\mathrm{tr}\left(\nabla_{(\sigma)}\mathbf{n}\right)\right) \quad (5)$$

$$\text{Rotation pressure} = -\sum_{j=1}^{m} 2j\mu_{2j}(\mathbf{n}\cdot\mathbf{k})^{2j-2} \times\left((2j-1)\mathbf{nn}:\nabla_{(\sigma)}\mathbf{k} + 2(\mathbf{n}\cdot\mathbf{k})^{2}H\right) \quad (6)$$

Here, H is the mean curvature. We denote dimensionless anchoring coefficients by $\varepsilon_{2j} = \mu_{2j}/\gamma_0$ ($j = 1,\ldots, m$). The dimensionless spatial parameters are scaled by the cholesteric pitch P_0. For example, $\mathbf{x}^\star = \mathbf{x}/P_0$ and $\nabla^\star = P_0\nabla$. The three capillary pressures add to zero for an open surface at equilibrium[55,60] and define the "easy shape" geometry of a LC surface.[119] The governing equation is a second-order nonlinear partial differential equation (PDE)

$$\begin{aligned} 0 = & -2H^*\left(1+\sum_{j=1}^{m}\varepsilon_{2j}(\mathbf{n}\cdot\mathbf{k})^{2j}\right) \\ & +\sum_{j=1}^{m} 2j\varepsilon_{2j}(\mathbf{n}\cdot\mathbf{k})^{2j-2}\left((2j-1)\mathbf{kn}:\nabla^*_{(\sigma)}\mathbf{n} + (\mathbf{n}\cdot\mathbf{k})\mathrm{tr}\left(\nabla^*_{(\sigma)}\mathbf{n}\right)\right) \\ & +\sum_{j=1}^{m} 2j\varepsilon_{2j}(\mathbf{n}\cdot\mathbf{k})^{2j-2}\left((2j-1)\mathbf{nn}:\nabla^*_{(\sigma)}\mathbf{k} + 2(\mathbf{n}\cdot\mathbf{k})^{2}H^*\right) \end{aligned} \quad (7)$$

A flat surface ($\mathbf{k}$ is a constant vector) is not a solution to eqn (7). Therefore, an anchoring-driven cholesteric liquid crystal surface has the tendency to wrinkle (creating nonvanishing $\nabla_{(\sigma)}\mathbf{k}$ to compensate $\mathbf{n}$ and $\nabla_{(\sigma)}\mathbf{n}$ effect). We study the surface wrinkling profile of chiral liquid crystals and impose a periodic boundary condition at $x^\star = 0$ and $x^\star = 1$, as well as at $y^\star = 0$ and $y^\star = 1$. The director field used here takes a spherical coordinate parametrization:[55]

$$\mathbf{n} = \begin{bmatrix} \sin ax^* \cos by^* \\ \sin by^* \\ \cos ax^* \cos by^* \end{bmatrix} \quad (8)$$

Without introducing asymmetry into $x^\star$ and $y^\star$, assuming that $a = b = 2\pi$, $\mathbf{n}$ represents the director field of a double periodic cholesteric liquid crystal. In this manuscript, we expect to observe quantities with at least one periodicity due to the special director field. Other director fields and their effects were studied in ref. 55. Eqn (8) is chosen as a representative director field with sufficient geometric richness, and within the scope and objectives of this paper.

2.2 Linear model of surface wrinkling

Observations show that surface wrinkling in nature is usually in the scale of nanometres, while the helix pitch is in the range of micrometers,[22,49–52] indicating the presence of a small parameter in the shape eqn (7). Hence under a small wrinkling approximation ($|\varepsilon_{2j}| \ll 1$), the shape eqn (7) can be linearized. The simplified eqn (7) is solvable by the spectral method, which gives the solution as a linear combination of distinct $\cos 2\pi\omega_{x^*}x^*$ $\cos 2\pi\omega_{y^*}y^*$ fundamental wrinkling modes. We denote those wrinkling modes as $\langle\omega_{x^*}, \omega_{y^*}\rangle$ for simplicity in this paper and in the ESI.† The linear solution under the Monge parametrization $h^\star = h^\star(x^\star, y^\star)$ can be written as (mathematical details are included in Sections S3 and S4 of ESI†):

$$h_l^* = -\frac{\varepsilon_2}{\pi}\mathbf{w}_{x^*}^{\mathrm{T}}\left(\sum_{j=1}^{m} jr_{j-1}\mathbf{Q}_{2j}\right)\mathbf{w}_{y^*} - c_{\mathrm{m}} \quad (9)$$

where $r_j = \varepsilon_{2(j+1)}/\varepsilon_2$ (define $r_0 = 1$) represent the dimensionless ratios of the anchoring coefficient $\varepsilon_{2(j+1)}$ and the second order anchoring coefficient. c_m is an integration constant and shifts h_l^* to a surface profile of zero mean. $\mathbf{w}_{x^*}$ and $\mathbf{w}_{y^*}$ are the wrinkling vectors along the coordinates $x^\star$ and $y^\star$ coordinates:

$$\mathbf{w}_{x^*} = \begin{bmatrix} \cos 0 \\ \cos x^* \\ \cdots \\ \cos(2m-1)x^* \\ \cos 2mx^* \end{bmatrix}_{2m+1}, \quad \mathbf{w}_{y^*} = \begin{bmatrix} \cos 0 \\ \cos y^* \\ \cdots \\ \cos(2m-1)y^* \\ \cos 2my^* \end{bmatrix}_{2m+1} \quad (10)$$

The $\mathbf{Q}_{2j}$-matrix in eqn (9) contains $(2j+1)\times(2j+1)$ entries and its (a, b)-element represents a wrinkling mode of $\langle a-1, b-1\rangle$. $\mathbf{Q}$-Matrices are constant sparse matrices, for example,

$$\mathbf{Q}_2 = \begin{bmatrix} 0 & 0 & 0 \\ 0 & 0 & 1/5 \\ 1/8 & 0 & 1/16 \end{bmatrix}, \quad \mathbf{Q}_4 = \begin{bmatrix} 0 & 0 & 0 & 0 & 0 \\ 0 & 0 & 3/40 & 0 & 3/136 \\ 3/64 & 0 & 1/32 & 0 & 1/320 \\ 0 & 0 & 1/104 & 0 & 1/200 \\ 3/256 & 0 & 1/80 & 0 & 1/512 \end{bmatrix}$$

The calculation details and numerical methods of $\mathbf{Q}$-matrices are given in the ESI.†

Eqn (7) shows a translational symmetry $h^\star \to h^\star + c$, and as above-mentioned the constant c is chosen such that the average mean value of $h^\star$ profile is zero, which furthers simplifies the calculation of the surface roughness discussed in Section 3.

In conclusion, the linear solution h_l^* can be compactly rewritten as:

$$h_l^* = \underbrace{\left(-\frac{\varepsilon_2}{\pi}\right)}_{\text{amplitude}} \mathbf{w}_{x^*}^{\mathrm{T}} \underbrace{\mathbf{C}(r_1, r_2, \ldots)}_{\text{morphology matrix}} \mathbf{w}_{y^*} - \underbrace{c_m(\mathbf{C})}_{\text{average mean shift}} \tag{11}$$

where the morphology matrix $\mathbf{C} = \sum j r_{j-1} \mathbf{Q}_{2j}$ is the summation of the weighted **Q**-matrices and is only dependent to the anchoring ratios r_j. In eqn (11), the amplitude is only dependent to the second order anchoring coefficient ε_2; the average mean shift is a constant determined by the morphology matrix **C**; the morphology of the wrinkling profile is controlled by the anchoring coefficient ratios $r_1, r_2, \ldots$ Fig. 2(a) shows a representative visualization of constant **Q**-matrices (see ESI†). Each element in the matrix represents a distinct wrinkling mode. Fig. 2(b) is the wrinkling mode $\langle 1, 2\rangle$, which corresponds to the second row and third column (dark red) of each **Q**-matrix.

All elements in a **Q**-matrix are non-negative, hence **Q**-matrices can be normalized by $\mathbf{Q}^* = \mathbf{Q} \Big/ \sum_{i,j} Q_{ij}$ such that each element represents the weight of the total elements. In Fig. 2(a), the dominating three principal wrinkling modes for each matrix are (1) biaxial wrinkling $\langle 1, 2\rangle$, shown in dark red colour; (2) equibiaxial wrinkling $\langle 2, 2\rangle$, shown in green-cyan colour and (3) uniaxial wrinkling $\langle 2, 0\rangle$, shown in yellow colour. The other wrinkling modes, corresponding to higher order harmonic waves, contribute much less than the three principal modes. This pattern remains the same from $\mathbf{Q}_2^*$ to $\mathbf{Q}_8^*$. The linear combination of $\mathbf{Q}_{2j}^*$ with coefficient of r_{j-1} (which is **C**-matrix) shows an anchoring ratio-independent feature of three dominating wrinkling modes: $\langle 1, 2\rangle$, $\langle 2, 2\rangle$, and $\langle 2, 0\rangle$.

In this paper, we study the 6th-order Rapini-Rapoular model numerically and expand the results to a generalized 2*m*th-order model. In a 6th-order anchoring mode, the characteristic lines in the parametric space (r_1, r_2) are shown in Fig. 3. These characteristic lines, and the vanishing modes are summarized

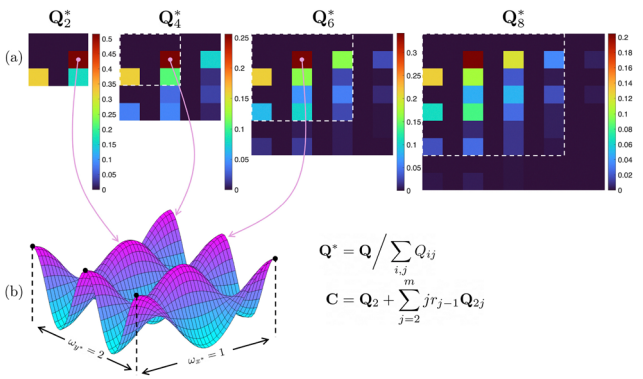

Fig. 2 (a) Visualization of **Q***-matrix where the colour represents the weight of each wrinkling modes in a **Q**-matrix. The dash line encircles the location of previous **Q***-matrix. The index (*i*, *j*) of each **Q***-matrix corresponds to a unique wrinkling mode with $\omega_{x^*} = (i-1)$ and $\omega_{y^*} = (j-1)$. For example, the (2, 3) component of each **Q***-matrix represents a wrinkling mode $\cos 2\pi(2-1)x^* \cos 2\pi(3-1)y^*$ described by (b).

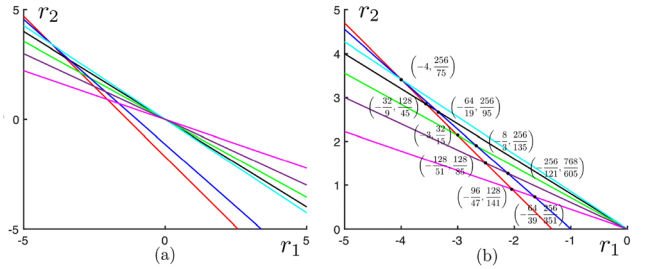

Fig. 3 (a) Characteristic lines in the parametric space (r_1, r_2); (b) expansion around negative r_1 values. Along each characteristic line, one wrinkling mode vanishes.

in Table 1. r_1 and r_2 are constrained by ε_2 since a thermodynamic stability requires $\gamma^* > 0$. The details are discussed in Section S2 of ESI.†

The wrinkling modes $\langle \omega_{x^*}, \omega_{y^*}\rangle$ can be categorized into three groups: (1) uniaxial wrinkling (if $\omega_{x^*}\omega_{y^*} = 0$); (2) equibiaxial wrinkling (if $\omega_{x^*}\omega_{y^*} \neq 0$ and $\omega_{x^*} = \omega_{y^*}$); or (3) biaxial wrinkling (if $\omega_{x^*}\omega_{y^*} \neq 0$ and $\omega_{x^*} \neq \omega_{y^*}$). A pure uniaxial wrinkling mode represents a developable surface where Gaussian curvature vanishes everywhere. A pure equibiaxial wrinkling mode represents an ideal egg-carton surface, where x^* and y^*-axes are symmetric. In nature, most surfaces are biaxial. In Table 1, if $r_2 = -(4/5)r_1$, the uniaxial mode $\langle 4, 0\rangle$ and biaxial mode $\langle 1, 4\rangle$ vanish, and the surface is a linear combination of 19 different wrinkling modes (see Section S4 of ESI†).

2.3 Surface roughness characterization

In this section, we present and discuss the definitions for all the surface roughness characterizations and parameters studied in this paper and summarize them into Table 2. In the following, we categorize the surface roughness into three methods: (1) curvature; (2) higher-order moments; (3) autocorrelation. Results using the three methods will be discussed in Sections 3.2.1, 3.2.2 and 3.2.3 respectively.

Next we discuss the definitions and nomenclature introduced in Table 2.

1. The surface curvatures are defined by the components of curvature tensor $\mathbf{B} = -\nabla_{(\sigma)}^* \mathbf{k}$. The usual curvatures are mean

Table 1 Characteristic lines and the vanishing modes (Fig. 3)

Characteristic lines	Colour	Vanishing modes	Category
$r_2 = -\frac{96}{75} r_1 - \frac{128}{75}$	Red	$\langle 2,0\rangle + \langle 1,2\rangle$	Uniaxial + biaxial
$r_2 = -\frac{4}{5} r_1$	Black	$\langle 4,0\rangle + \langle 1,4\rangle$	Uniaxial + biaxial
$r_2 = -\frac{256}{225} r_1 - \frac{256}{225}$	Blue	$\langle 2,2\rangle$	Equibiaxial
$r_2 = -\frac{4}{9} r_1$	Magenta	$\langle 4,4\rangle$	Equibiaxial
$r_2 = -\frac{32}{45} r_1$	Green	$\langle 2,4\rangle + \langle 4,2\rangle$	Biaxial
$r_2 = -\frac{64}{75} r_1$	Cyan	$\langle 3,2\rangle$	Biaxial
$r_2 = -\frac{8}{15} r_1$	Purple	$\langle 3,4\rangle$	Biaxial

curvature $H^\star = \mathrm{tr}\,\mathbf{B}/2$ and the Gaussian curvature $K^\star = \det \mathbf{B}$. The deviatoric curvature is $D^* = \sqrt{H^{*2} - K^*} > 0$ (deviation from a sphere) and the Casorati curvature $C^* = \sqrt{H^{*2} + D^{*2}}$ (deviation from a flat plane). The dimensionless shape parameter $S = (2/\pi)\arctan(H^\star/D^\star)$ is a normalized shape index that takes value between -1 to $+1$. The three primitive shapes are sphere ($S = \pm 1$), cylinder ($S = \pm 0.5$) and saddle ($S = 0$). The signs correspond to concave up or down. These curvatures are further discussed in our previous work[145–147] but we emphasize that the (C, S) description separates shape and curvedness properties while the standard (H, K) geometric formulation co-mingles shapes and curvedness but if the main focus is shape description or curvedness description then the (C, S) methodology is preferable.

All the curvatures defined previously can also be written in terms of two principal curvatures: a larger curvature κ_1^* and a smaller curvature κ_2^*.

$$H^* = \frac{\kappa_1^* + \kappa_2^*}{2},\ D^* = \frac{\kappa_1^* - \kappa_2^*}{2},\ K^* = \kappa_1^*\kappa_2^* \tag{12}$$

$$C^* = \sqrt{\frac{\kappa_1^{*2} + \kappa_2^{*2}}{2}},\ S = \frac{2}{\pi}\arctan\left(\frac{\kappa_1^* + \kappa_2^*}{\kappa_1^* - \kappa_2^*}\right) \tag{13}$$

These expressions offer a more intuitive image. For example, traditional curvatures such as $H^\star$, $D^\star$ and $K^\star$ measure the arithmetic mean, sphericity, and the geometric mean without considering the sign, respectively. The novel Casorati curvature $C^\star$ captures the magnitude of the two principal curvatures, while the shape parameter S is naturally a dimesionless quantity that describes the shape of a surface patch within a small neighbourhood. Other details of the these curvatures in a tensorial approach or in a principal curvature language can be found in literature.[146]

Since curvature is a quantity defined on a single point, we introduce an average quantity $\overline{P^{*2}}$ to measure the average curvature magnitude with respect to the $P^\star$-curvature by

$$\overline{P^{*}} = \frac{1}{A^*}\iint_\Omega P^* \mathrm{d}A^*, \quad P = H^2, D^2, C^2, K \tag{14}$$

In this paper, $\overline{C^{*2}} = 2\overline{H^{*2}} = 2\overline{D^{*2}}$ and $\overline{K^*} = 0$ as restricted by the Gauss–Bonnet theorem.[148–150] Hence, minimizing $\overline{C^{*2}}$ is equivalent to minimizing $\overline{H^{*2}}$ (Helfrich elastic energy[93–95]) or $\overline{D^{*2}}$ (Willmore energy[90–92]). In the following content, to investigate the average curvature, we only need to consider the mean curvature $\overline{H^{*2}} \geq 0$. The average magnitude of mean curvature $\overline{H^{*2}}$ can be calculated with the linear approximation of the surface profile in eqn (11). For example, the mean curvature can be calculated with $H^* \approx \frac{1}{2}\mathrm{tr}\nabla^*\nabla^* h^* = 2\varepsilon_2\pi C_{ij}\big((i-1)^2 + (j-1)^2\big)\langle i-1, j-1\rangle$. The average magnitude of the mean curvature is therefore

$$\begin{aligned}\overline{H^{*2}} &= \frac{1}{A^*}\iint_\omega \sqrt{g}H^{*2}\mathrm{d}x^*\mathrm{d}y^* \\ &= \varepsilon_2{}^2\pi^2 \sum_{i,j,a,b=1} C_{ij}C_{ab}\big((i-1)^2 + (j-1)^2\big)\big((a-1)^2 + (b-1)^2\big)\end{aligned} \tag{15}$$

$$\big(\delta^0_{i+a-2} + \delta^0_{i-a}\big)\left(\delta^0_{j+b-2} + \delta^0_{j-b}\right) + \mathcal{O}\left(|\nabla^* h^*|^2\right) \tag{16}$$

The details are included in Section S5 of ESI.† Here, δ is the Kronecker delta, and i, j, a, b are indices of summation. Matrix C_{ij} is defined in eqn (11) and the values are given in Section S4 of ESI.† This is a very important result because eqn (16) provides a direct relation between the average mean $\overline{H^{*2}} = \overline{H^{*2}}(r_1, r_2, \ldots)$, where the anchoring ratios (r_1, r_2, …) are encapsulated inside the C_{ij}-matrices.

2. The average curvature magnitude $\overline{H^{*2}}$ is defined only if the surface is smooth. A more general approach is to consider the higher-order moments. The first-order moment (mean), second-order moment (root mean square), third-order moment (skewness) and fourth-order moment (kurtosis) are the most applicable features of a surface profile. The first-order moment is zero since it is the condition to determine c_m value in eqn (11). For a mean-free surface profile, the root mean square (Sq), surface skewness (Rsk) and kurtosis (Rku) are defined by the following equations (details are included in Section S6 of ESI†):

$$\mathrm{Sq} = \sqrt{\frac{1}{A^*}\iint_\Omega h^{*2}\mathrm{d}A^*} \approx \left|\frac{\varepsilon_2}{\pi}\right|\sqrt{\mathrm{tr}(\mathscr{A}\cdot\mathbf{C}\cdot\mathscr{A}\cdot\mathbf{C}^{\mathrm{T}})} \tag{17}$$

$$\mathrm{Rsk} = \frac{1}{A^*\mathrm{Sq}^3}\iint_\Omega h^{*3}dA^* \approx -sgn(\varepsilon_2)\frac{C_{ab}C_{ij}C_{kl}\mathscr{A}_{aik}\mathscr{A}_{bjl}}{(\mathrm{tr}(\mathscr{A}\cdot\mathbf{C}\cdot\mathscr{A}\cdot\mathbf{C}))^{3/2}} \tag{18}$$

$$\mathrm{Rku} = \frac{1}{A^*\mathrm{Sq}^4}\iint_\Omega h^{*4}\mathrm{d}A^* \approx \frac{C_{ab}C_{ij}C_{km}C_{np}\mathscr{A}_{aikn}\mathscr{A}_{bjmp}}{(\mathrm{tr}(\mathscr{A}\cdot\mathbf{C}\cdot\mathscr{A}\cdot\mathbf{C}^{\mathrm{T}}))^2} \tag{19}$$

where high-order sparse matrix A is defined by

$$\mathscr{A}_{abc..} = \int_0^1 \cos 2\pi(a-1)x^* \cos 2\pi(b-1)x^* \cos 2\pi(c-1)x^* \ldots \mathrm{d}x^* \tag{20}$$

Table 2 Table of all the surface roughness parameters discussed in this paper. Their nomenclature, range of value, corresponding section, requirement for surface profile and the physical significance are included

Surface roughness parameter	Nomenclature	Range	Section	Surface profile ($h^\star$)	Significance
Average magnitude of curvature	$\overline{H^{*2}}$	≥ 0	3.2.1	Twice differentiable	Total Willmore/Helfrich energy
Root mean square	Sq	≥ 0	3.2.2	No requirement	Standard deviation
Skewness	Rsk	$\mathbb{R}$	3.2.2	No requirement	Degree of bias of the roughness profile
Kurtosis	Rku	≥ 0	3.2.2	No requirement	Sharpness of roughness profile
Autocorrelation function	acf	$1 \geq \mathrm{acf} \geq -1$	3.2.3	No requirement	Surface self-convolution
Autocorrelation length	Sal	$1 > \mathrm{Sal} > 0$ or $\varnothing$	3.2.3	No requirement	High/low frequency dominated

3. The method of higher-order moments focuses on the h-direction, while the autocorrelation length takes the information along x^* and y^* direction, and it is irrelevant to the surface height. In partial summary, the autocorrelation function (acf) and autocorrelation length (Sal) are determined by the frequency of wrinkling modes.[151] The normalized autocorrelation function (acf) measures how similar the solution is compared to its lagged copy. Intuitively, a smooth surface has a low acf for every lagging $(\Delta x^*, \Delta y^*)$.[152–154] In linear region, the acf function is a convolution of the surface profile and itself $\mathrm{acf}(\Delta x^*, \Delta y^*) = h^{**}h^*$, where $*$ is the 2D convolution operator.

$$\begin{aligned}\mathrm{acf} &= \frac{1}{A^*\mathrm{Sq}^2}\iint_{\Omega}\sqrt{g}h^*(x^*,y^*)h^*(x^*-\Delta x^*,y^*-\Delta y^*)\mathrm{d}x^*\mathrm{d}y^*\\ &\approx\frac{\sum_{i,j,a,b} C_{ij}C_{ab}\mathscr{A}_{ia}\mathscr{A}_{jb}}{\mathrm{tr}(\mathscr{A}\cdot\mathbf{C}\cdot\mathscr{A}\cdot\mathbf{C}^{\mathrm{T}})}\cos 2\pi(a-1)\Delta x^*\cos 2\pi(b-1)\Delta y^*\end{aligned} \tag{21}$$

where the constant related to c_m is neglected (derivation is given in Section S6 of ESI†). The value $\mathrm{acf}(0, 0) = 1$ is a property independent to the surface profile. The autocorrelation length Sal is defined by as the smallest spatial translation that renders acf to a specific value c. Mathematically, $\mathrm{Sal} = \min\sqrt{\Delta x^{*2} + \Delta y^{*2}}$ such that $\mathrm{acf} = c$.[84] In this manuscript, we adopt $c = 0$ for achieving uncorrelated conditions.

3 Results

3.1 Direct numerical simulations

Numerical simulations of the nonlinear shape eqn (7) were performed with periodic boundary conditions. We use a pseudo-transient approach to solve this nonlinear PDE by introducing an additional time dimension t^* and let $t^* \to +\infty$.[155,156] Once the surface profile converges, the average value cm is calculated numerically as imposed by the vanishing mean condition. The dimensionless relative error for this iterative approach is defined as $\mathrm{error} = 100\% \times \|h^{*j+1} - h^{*j}\|/\|h^{*j}\|$, where h^{*j} represents h^* at the jth time step. We adapt a finite difference approach on the space and an explicit Euler approach on the time dimension. Due to the regularity of the heat operator $\partial_{t^*} - \nabla^{*2}$ and the periodic boundary condition, the initial condition can be chosen randomly. The Courant–Friedrichs–Lewy condition is modified specifically for this nonlinear PDE by $\Delta t^* = (\alpha/4)\cdot(\Delta x^*)^2$, where $\alpha = 0.1$ for a fast and stable calculation. Fig. 4 shows the numerical solution of a surface wrinkling under $\varepsilon_2 = -0.1$, $\varepsilon_4 = +0.08$ and $\varepsilon_6 = -0.06$.

To confirm that the algorithm is irrelevant to the distribution and magnitude of the initial guess, we adopt a random field multiplied by a magnitude factor. Fig. 4(a) adopts a much smaller initial guess $\sim 10^{-5}|\varepsilon_2/\pi|$ while Fig. 4(b) uses an initial guess $\sim|\varepsilon_2/\pi|$. The simulations with different initial guesses converge to the same solution (Fig. 4(e)). Fig. 4(c) and (d) are the iteration-error plots for Fig. 4(a) and (b), respectively. Comparing Fig. 4(c) and (d), we see that if the initial guess is very far from the real solution, the iterative method is overly slow ($\sim 10^6$ steps to converge) and the initial error becomes

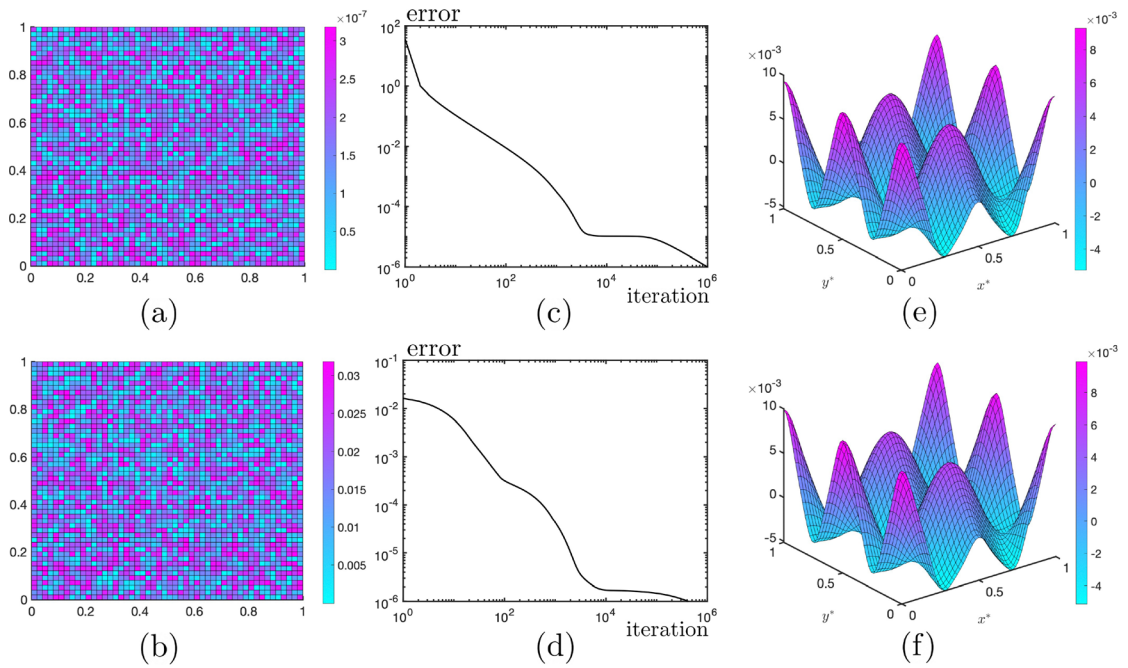

Fig. 4 Numerical simulations performed on a 51 × 51-grid, with dimensionless anchoring parameters $\varepsilon_2 = -0.1$, $\varepsilon_4 = +0.08$ and $\varepsilon_6 = -0.06$. The iteration terminates if the dimensionless relative error reaches $\delta = 10^{-6}$. (a) Initial condition $h_{\mathrm{initial}} = 10^{-5}|\varepsilon_2/\pi|\mathrm{rand}(0,1)$; (b) initial condition $h_{\mathrm{initial}} = |\varepsilon_2/\pi|\mathrm{rand}(0,1)$; (c) and (d) are the iteration-error plot when the simulation starts at initial condition (a) and (b), respectively; (e) the converged numerical solution; (f) the linear approximation.

much larger ($\sim 10^2$). Fig. 4(f) is the analytic solution obtained from eqn (11). Comparing Fig. 4(e) and (f), we conclude that the analytic approximation gives a very precise approximation to the numerical solution.

3.2 Surface roughness

In this section, we study the surface roughness of the wrinkling profile discussed in Section 3.1 (see representative result of Fig. 4(e)). Table 2 summarizes all surface roughness parameters studied in this section.

3.2.1 Curvature profiles. Fig. 5 shows the heat map of $\overline{H^{*2}} = \overline{H^{*2}}(r_1, r_2)$. The curve of minima follows a straight line (black line) given by $r_2 = -0.7793r_1 - 0.338$. The global minimum $\left(\min\left\{\overline{H^{*2}}\right\} = 0.0643\right)$ is found when $r_1 = -1.43$ and $r_2 = 0.78$.

Fig. 5 shows that the wrinkling profile without higher-order harmonics ($r_1 = r_2 = 0$) does not show a minimized average curvature $\left(\min \overline{H^{*2}}\right)$. Following a linear relation $r_2 = -0.7793r_1 - 0.338$ and introducing higher-order harmonics reduces the average magnitude of curvature. Since the linear relation is a straight line that does not pass the first quadrant, the minimum cannot be reached when the anchoring coefficients ε_2, ε_4, and ε_6 are of the same sign. The global minimum ($r_1 = -1.43$, $r_2 = +0.78$) reveals that to obtain a small average magnitude of curvature, the anchoring coefficients should alternate their signs such that $\mathrm{sgn}(\varepsilon_2, \varepsilon_4, \varepsilon_6) = (+, -, +)$ or $(-, +, -)$.

These important observations can be verified from the linear approximation. Minimizing $\overline{H^{*2}}$ with respect to either r_1 or r_2 requires linear calculations of $C_{ab}(\partial C_{ij}/\partial r)$, which is a linear function of r_1 and r_2. Therefore, the linear approximation confirms that there exists a linear function that minimizes the average magnitude of mean curvature. The linear approximation also verifies that $\overline{K^{*2}} = 0$, where details are given in the ESI.† For clarity, we refer to surface with a minimum $\overline{H^{*2}}$ as the $\min\left\{\overline{H^{*2}}\right\}$ surface. Table 3 summarizes the numerical results and the linear approximation for the $\min\left\{\overline{H^{*2}}\right\}$ surface, and Fig. 6 shows the direct numerical simulations for $\min\left\{\overline{H^{*2}}\right\}$ surface.

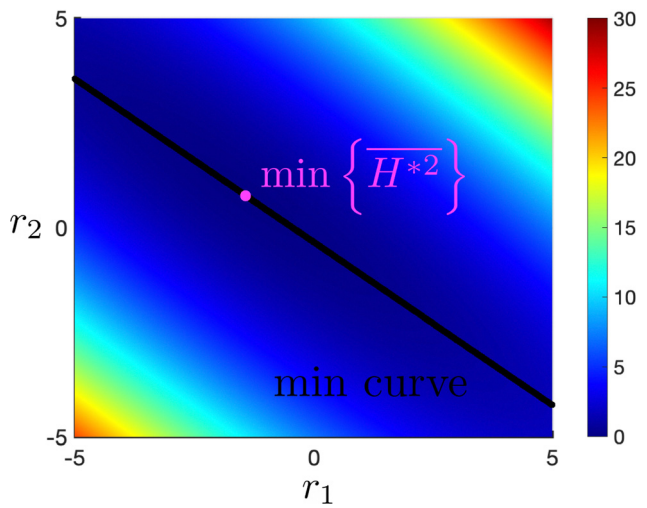

Fig. 5 The analytic result of the average magnitude of mean curvature $\overline{H^{*2}} = \overline{H^{*2}}(r_1, r_2)$ defined in eqn (14). The minimum curve follows a straight line $r_2 = -0.7793r_1 - 0.3380$. The global minimum (white point) is achieved when $r_1 = -1.43$ and $r_2 = 0.78$, with corresponding value $\min\left\{\overline{H^{*2}}\right\} = 0.0643$.

Fig. 6(a) and (b) show the analytic solution and the direct numerical simulation of the $\min\left\{\overline{H^{*2}}\right\}$ surface, respectively. Fig. 6(c) shows the top view of the numerical solution. The dimensionless (scaled by P_0) mean curvature H^*, Gaussian curvature K^*, deviatoric curvature D^*, Casorati curvature C^* and normalized shape parameter S of the $\min\left\{\overline{H^{*2}}\right\}$ surface are shown in Fig. 6(d)–(h), respectively. Comparing Fig. 6 and 4, we conclude that the $\min\left\{\overline{H^{*2}}\right\}$ surface demonstrates few surface kinks near the boundary. Intuitively, the emergence of kinks introduces extra surface patches with low magnitude of curvature. This intuition matches Fig. 6(d), where green semi-rings ($H^{*2} = 0$) appear around those kinks. This intuition is also confirmed by the dark blue semi-rings ($D^{*2} = 0$) in Fig. 6(f). The $\min\left\{\overline{H^{*2}}\right\}$ surface demonstrates complex curvature profiles shown in Fig. 6, with topological constraint that surface integral of those curvatures must satisfy $\overline{K^*} = 0$, and $\overline{C^{*2}} = 2\overline{H^{*2}} = 2\overline{D^{*2}}$. In addition, if we compare Fig. 6(d) and (e) with (g) and (h) we see that separating curvedness (C^*) from shape (S) show directly where we have saddles ($S = 0$), cylinder ($S = \pm 1/2$), and spheres ($S = \pm 1$), and what is the curvedness at the geometric transitions between these shapes. Fig. 6 demonstrates that the higher-order anchoring model together with a doubly-periodic director field is a generator of periodic surface patterns with a rich distribution of saddles, cups/domes, and saddles with a distribution of large and small curvedness patches as required in highly functional topographies.

In partial summary, $\overline{H^{*2}}$ is a good indicator to describe the surface roughness by evaluating the curvature distribution of each point. The linear approach given in eqn (11) is not only a good approximation of the surface profile h^*, but also a good approximation of its second derivative (validated in Table 3). The advantage of $\overline{H^{*2}}$-method is that $\overline{H^{*2}}$ has physical significance (such as the Willmore energy or the Helfrich energy), and the disadvantage is that the surface equation must be at least

Table 3 Analytic and numerical results of global minimum surface (Fig. 6)

Surface parameter	Analytic result	Numerical result
$\iint_\Omega H^{*2} \mathrm{d}A^*$	0.0643	0.0567
$\iint_\Omega D^{*2} \mathrm{d}A^*$	0.0643	0.0566
$\iint_\Omega K^* \mathrm{d}A^*$	0	5.5×10^{-5}
$\iint_\Omega C^{*2} \mathrm{d}A^*$	0.1286	0.1133
Rsk	0.3217	0.2265
Rku	2.1024	2.1124

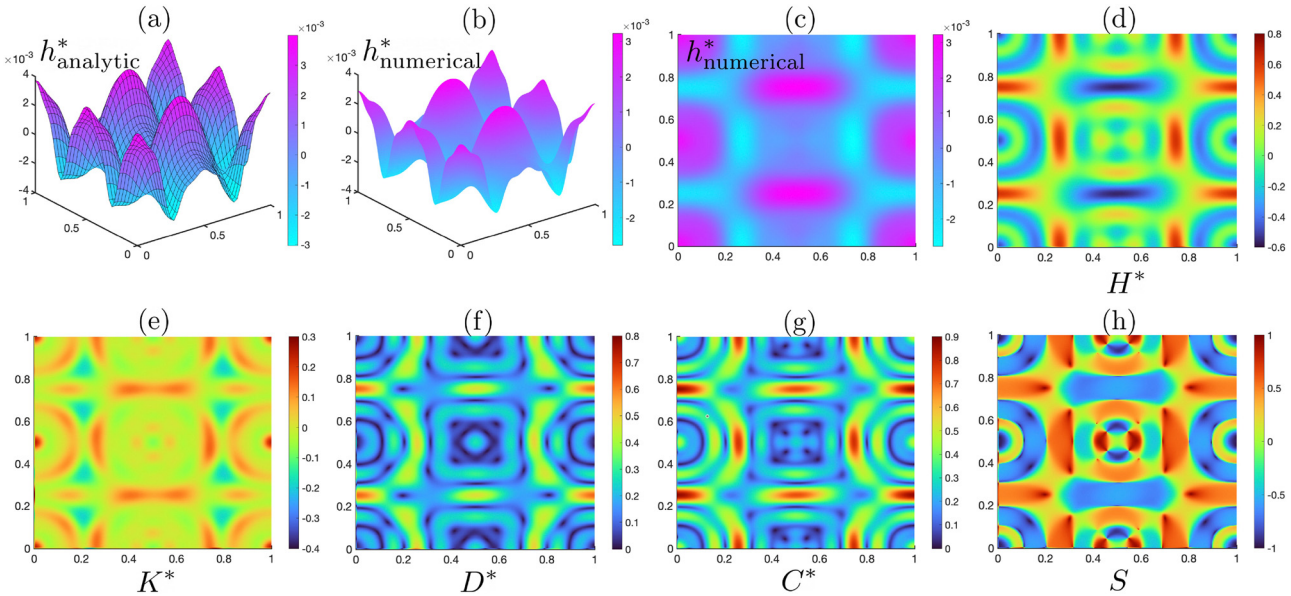

Fig. 6 Numerical simulation for surface with $\varepsilon_2 = -0.1$, $r_1 = -1.43$, and $r_2 = 0.78$. (a) Is the analytic approximation of the surface. (b) Is the numerical simulation performed on a 251 × 251-grid with tolerance $\delta = 10^{-6}$. (c) Is the (x^*, y^*) heat map of (b). (d)–(h) Are the dimensionless curvature heat map plots of the numerical surface profile. (d)–(h) Are the dimensionless mean curvature H^*, dimensionless Gaussian curvature K^*, dimensionless deviatoric curvature D^*, dimensionless Casorati curvature C^* and the dimensionless shape parameter S, respectively. The calculated average curvatures are $\overline{C^{*2}} = 0.1133$, $\overline{H^{*2}} = 0.0567$, $\overline{D^{*2}} = 0.0566$, and $(1/A^*)\int\int_\Omega K^* \mathrm{d}A^* = 5.5044 \times 10^{-5}$. These values are summarized in Table 3.

twice differentiable. Lastly, with a representative result of surface roughness in a CLC given in Fig. 6, we demonstrate that the generalized higher-order liquid crystal shape equation has the potential to generate complex roughness, with distributed saddles, cups/domes, and cylindrical shapes, which can be fine-tuned by anchoring coefficients and surface director orientation. This parametric tuning is performed in detail through roughness calculations of biological surfaces and summarized in Table 4 later in Section 3.3.

3.2.2 Higher-order moments. In this section, we study the higher-order moments of surface wrinkling defined in eqn (17)–(19). We used linear approximations of eqn (17)–(19) to calculate how the anchoring coefficient ratios (r_1, r_2) change the surface roughness. In eqn (17), the root mean square Sq is dependent to the magnitude factor $|\varepsilon_2/2\pi|$, while the magnitude of Rsk and Rku are independent to ε_2. ε_2 only changes the sign of Rsk and Rku is always non-negative. To generalize the discussion, we rescale Sq by $(\pi \mathrm{Sq}/\varepsilon_2)^2$. Fig. 7 shows how anchoring coefficient ratios affect higher-order moments.

In Fig. 7(a). $(\pi \mathrm{Sq}/\varepsilon_2)^2 \geq 0$ demonstrates a global minimum (white point) of 3.8742×10^{-4} at $r_1 = -2.92$ and $r_2 = +2.08$. The global minimum emerges due to the nature of a second-order polynomial $\mathbb{P}^2[r_1, r_2]$ in eqn (17). The surface kurtosis is a polynomial of the form $\mathbb{P}^4/\mathbb{P}^4$ from eqn (19). The complexity of the polynomial demonstrates an entangled Rku(r_1, r_2)-plot, shown in Fig. 7(d)–(f). Rku(r_1, r_2) is strictly non-negative and it demonstrates a global minimum. The global minimum of Rku is marked with a white point in Fig. 7(d). The global minimum min(Rku) = 1.8833 is reached when $r_1 = -2.86$ and $r_2 = +1.98$. Fig. 7(e) and (f) are the second and fourth quadrants of Fig. 7(d). In Fig. 7(d), we conclude that Rku changes rapidly near the global minimum.

The skewness is a polynomial of the form $\mathbb{P}^3/(\mathbb{P}^2)^{3/2}$, and the density map is shown in Fig. 7(b) and (c). We mark the two global minimum points that minimize Sq and Rku as white dots, and mark the point that minimizes $\overline{H^{*2}}$ (from Fig. 5) as a magenta dot in Fig. 7(b) and (c). The two global minimum points, minSq^2 and min{Rku} are located very close to each other, while min$\left\{\overline{H^{*2}}\right\}$ lays further. In Fig. 7(c), the green-cyan colour represents a skewness-free surface. The green-cyan boundaries start to diverge at the minSq^2 and min{Rku} points. And the global minimum point min$\left\{\overline{H^{*2}}\right\}$ is located inside a green-cyan region, showing a small Rsk value. The numerical value and analytic result are given in Table 3.

Table 4 Roughness characterization of biological examples based on the liquid crystal shape equation. Rsk, Rku and the corresponding r_1, r_2. The deviations are calculated by eqn (23)

Surface	(Rsk, Rku)	(r_1, r_2) if $\varepsilon_2 < 0$	(Δ_{Rsk}, Δ_{Rku}) if $\varepsilon_2 < 0$	(r_1, r_2) if $\varepsilon_2 > 0$	(Δ_{Rsk}, Δ_{Rku}) if $\varepsilon_2 > 0$
Trout with mucus (*Salmo trutta*)	(0.15, 3.3)	(−3.4068, 2.6338)	(-3.4×10^{-3}, -4×10^{-4})	(0.5386, −2.0672)	(-2.79×10^{-4}, -4.1×10^{-5})
Red maple leaf (*Acer rubrum*)	(0.42, 4.3)	(−3.4420, 2.7033)	(7.01×10^{-4}, 2.56×10^{-4})	(0.7490, −2.4101)	(6.5×10^{-5}, 2.5×10^{-5})
Back of hand (*Homo sapiens*)	(−0.19, 3.5)	(0.8355, −2.4307)	(-1.45×10^{-4}, -2.5×10^{-5})	(−3.4273, 2.6624)	(-4.86×10^{-4}, -5.6×10^{-5})
Flying lizard (*Draco timorensis*)	(0.56, 3.2)	(−2.2553, 1.6458)	(-2.4×10^{-5}, 5×10^{-6})	(−2.7490, 1.6366)	(1.63×10^{-4}, 6.2×10^{-5})

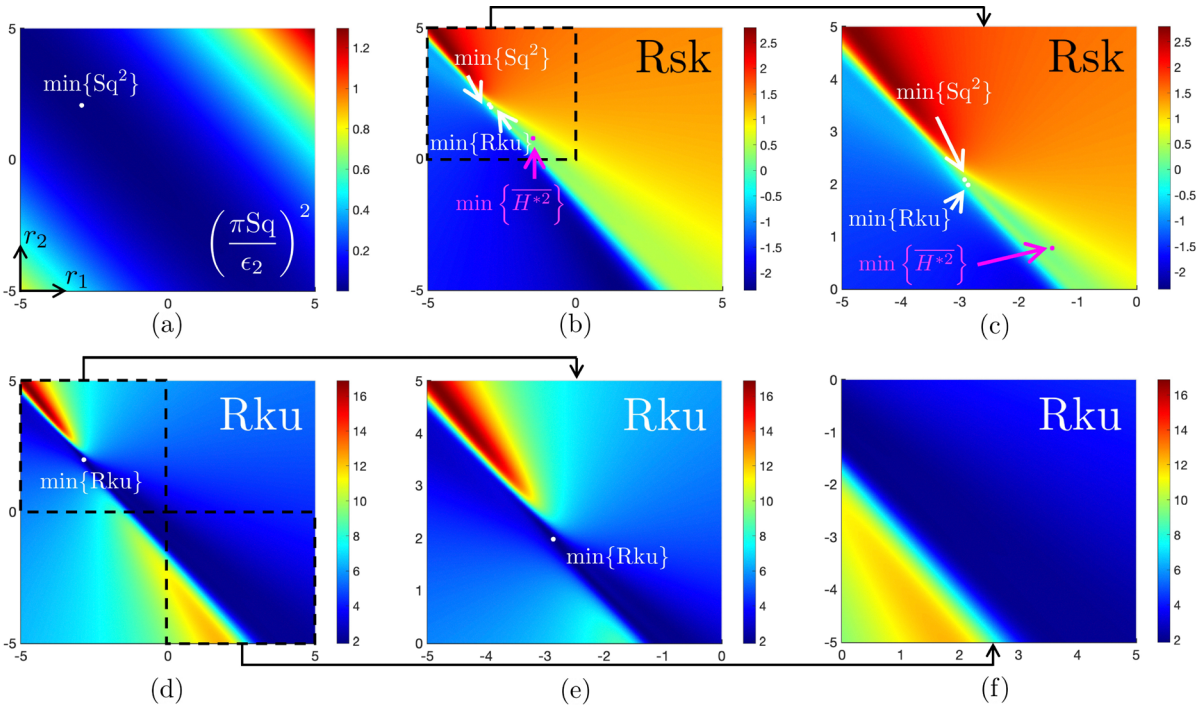

Fig. 7 The analytic result of surface roughness in the (r_1, r_2) parametric space. (a)–(d) Are the scaled $(\pi Sq/\varepsilon_2)^2$ plot, the skewness plot and the kurtosis plot for $(r_1, r_2) \in [-5, +5]^2$, respectively. (c) Shows the second quadrant of (b). (e) and (f) Show the second and the fourth quadrants of (d), respectively. The global minima for $(\pi Sq/\varepsilon_2)^2 > 0$ and $Rku > 0$ are marked with white dots. The $\min\{\overline{H^{*2}}\}$ surface is marked with a magenta dot. The location and the minimized values are: (a) $r_1 = -2.92$, $r_2 = +2.08$ and $\min\{(\pi Sq/\varepsilon_2)^2\} = 3.8742 \times 10^{-4}$. (d) $r_1 = -2.86$, $r_2 = +1.98$ and $\min\{Rku\} = 1.8833$.

According to the definition, the skewness and kurtosis are scaled by the root mean square and are dimensionless, which results a scale-independent Rsk–Rku plot shown in Fig. 8. The Rsk–Rku plot is widely used in surface manufacturing.[157,158] For example, Rsk ranges from −1 to + 1 for most surface machining process.[159] Fig. 8 shows a wide range of Rsk and Rku. There are two bounds in Fig. 8. The first bound $Rku \geq Rsk^2 + 1$ is an inequality resulting from the definition (derivation is given in the ESI,† where equality holds strictly for Bernoulli distributions[152,158,160]). The second bound $Rku \geq 1.8833$ is physical, which implies that it is impossible to obtain an anchoring-driven CLC surface with a lower Rku. The Rapini–Papoular anchoring model cannot generate a surface with low Rsk and high Rku. The intersections between the curves imply that an inverse problem does not have a unique solution, *i.e.*, different combination of r_1 and r_2 can generate a surface with the same Rku and Rsk. Other surface roughness parameters are required to determine the anchoring coefficients. The inverse problem will be discussed in Section 3.3.

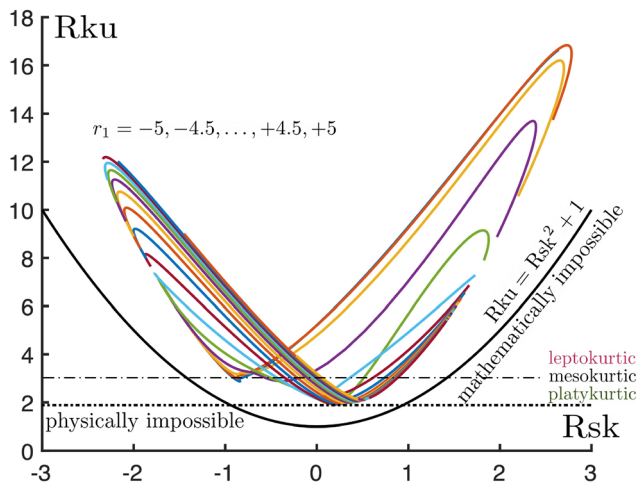

Fig. 8 The surface skewness and kurtosis plot. The curves are taken when $r_1 = -5, -4.5, \ldots, +5$. The region below the curve $Rku = Rsk^2 + 1$ is a mathematically impossible zone, and the region below $Rku < 1.8833$ is a physically impossible zone.

In partial summary, the method of higher-order moments evaluates the variance, bias and peakness of surface wrinkling. It shows that the Rapini-Rapoular model contains intrinsic bounds of root mean square and kurtosis. We also concluded that different anchoring coefficient ratios may result the same surface roughness parameters. To distinguish different surfaces with same Rsk and Rku, other methods should be incorporated. For example, introducing the 5th and 6th-order moment for calculating hyperskewness and hypertailedness.

3.2.3 Autocorrelation function and autocorrelation length. In this section, we study the autocorrelation function acf and the autocorrelation length Sal introduced in eqn (21).

Fig. 9(a)–(c) show the autocorrelation function acf as a function of lagging $(\Delta x^*, \Delta y^*)$ for the $\min\{(\pi Sq\varepsilon_2)^2\}$ surface, the $\min\{Rku\}$ surface, and the $\min\{\overline{H^{*2}}\}$ surface. The white

curves denote the region where acf function vanishes. The autocorrelation length Sal is the radius of the circle tangent to the closest white curve. Fig. 9(d) demonstrates the three regions of the **C**-matrix: the low-frequency block, the mid-frequency block and the high-frequency block. Comparing Fig. 9(b) and (c), the autocorrelation length for min{Rku} is Sal = 0.0703 which is smaller than that of the $\min\left\{\overline{H^{*2}}\right\}$ surface (Sal = 0.1691). Fig. 9(e) and (f) are the **C**-matrix visualization (scaled by $\sum_{i,j}|C_{ij}|$) of (b) and (c), where (c) is a low-frequency dominated profile (64.1%). Fig. 9 demonstrates that Sal is the proper surface roughness parameter that recognizes the frequency of the surface profile without considering the magnitude of the wrinkling.

In partial summary, autocorrelation function and autocorrelation length evaluate the correlation between the surface with its lagged copy. They are dependent to the (x^*, y^*)-direction and irrelevant to the h^*-direction. Noteworthy, larger Sal implies a surface that is dominated by low spatial frequency asperities, which agrees with the literature.[161]

3.3 Application and inverse problem

The skewness and kurtosis of a sample's surface profile are easier to measure compared to the anchoring coefficients. By solving the nonlinear eqn (18) and (19), this paper provides an alternative way to measure the anchoring coefficients. However, there are two concerns appearing in this approach. The first concern is that functions (18) and (19) are surjective-only, which are verified by Fig. 8. The intersections in Fig. 8 demonstrate that there is no unique pair of r_1 and r_2 that yield the given values of skewness and kurtosis. The second concern is that eqn (18) contains the sign of ε_2, and the final solutions are anchoring ratio vector $\mathbf{r} = [\,r_1 \quad r_2\,]^{\mathrm{T}}$, which is irrelevant to ε_2. To address the problem, we implement an optimization approach to find the anchoring coefficients that are closest to zero since the magnitude of those coefficients tend to be very small ($|\varepsilon_{2i}| \ll 1$). We can solve this inverse problem $\mathbf{F}(\mathbf{r}) = [\,\mathrm{Rsk}_0 \quad \mathrm{Rku}_0\,]^{\mathrm{T}}$ *via* a Levenberg–Marquardt algorithm with an updating formula

$$\Delta\mathbf{r} = -\left(\left(\frac{\partial\mathbf{F}}{\partial\mathbf{r}}\right)^{\mathrm{T}}\left(\frac{\partial\mathbf{F}}{\partial\mathbf{r}}\right) + \lambda\mathbf{I}_{2\times 2}\right)^{-1}\left(\frac{\partial\mathbf{F}}{\partial\mathbf{r}}\right)\cdot\left(\mathbf{F}(\mathbf{r}) - \begin{bmatrix}\mathrm{Rsk}_0\\ \mathrm{Rku}_0\end{bmatrix}\right) \tag{22}$$

Here, λ is the penalty parameter adjusted by each case, since an inverse problem usually involves a singular Jacobian matrix. If the error is below 10^{-6}, the method is switched to a Newton–Raphson method for a faster convergence rate. The calculation ends when

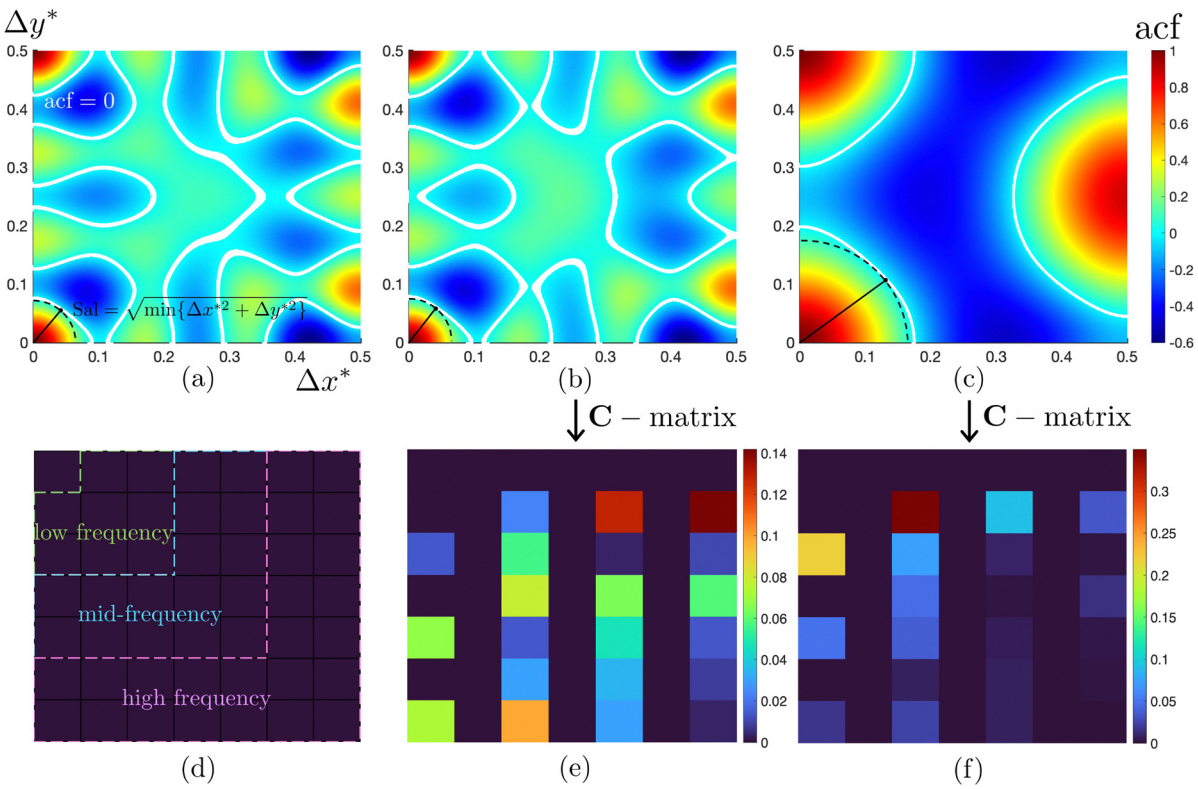

Fig. 9 Normalized autocorrelation function of (a) $\min\{(\pi\mathrm{Sq}/\varepsilon_2)^2\}$ point, $r_1 = -2.92$ and $r_2 = +2.08$. Sal = 0.0692 when (Δx^*, Δy^*) = (0.042, 0.055); (b) min{Rku} point, $r_1 = -2.86$ and $r_2 = +1.98$. Sal = 0.0703 when (Δx^*, Δy^*) = (0.045, 0.054); (c) $\min\left\{\overline{C^{*2}}\right\}$ point, $r_1 = -1.43$ and $r_2 = +0.78$. Sal = 0.1691 when (Δx^*, Δy^*) = (0.131, 0.107). From (a) to (c), white curves represent acf = 0. (d) **C**-Matrix can be split into three zones: low-frequency region, mid-frequency region, and high-frequency region. (e) The contribution heat map of the absolute value of each element in **C**-matrix for min{Rku} point (corresponding to (b)). The contribution ratio of each region is low : mid : high = 9.4 : 40.3 : 50.3. (f) The same **C**-matrix visualization for $\min\{\overline{C^{*2}}\}$ point (corresponding to (c)). The contribution ratio of each region is low : mid : high = 64.1 : 24.0 : 11.9. Comparing (e) and (f), we can observe that low frequency dominated profile (64.1%) shows a high Sal, while high frequency dominated profile (50.3%) shows a lower Sal.

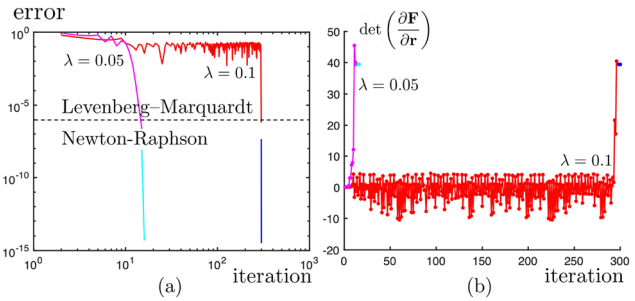

Fig. 10 (a) Convergence plot of the surface *Salmo trutta* by using different penalty factor λ. (b) Salmo trutta cannot be solved directly from Newton–Raphson method due to the singular Jacobian matrix. Large λ (such as $\lambda > 0.5$), small λ (such as $\lambda < 0.0001$) or inappropriate choice (such as $\lambda = 0.9$) lead to divergence.

error $< 10^{-9}$. The deviation is calculated once the converged $\mathbf{r}_c$ is obtained:

$$\Delta_{\mathrm{Rsk}} = \left(1 - \frac{\mathrm{Rsk}(\mathbf{r}_c)}{\mathrm{Rsk}_0}\right) \times 100\%, \qquad \Delta_{\mathrm{Rku}} = \left(1 - \frac{\mathrm{Rku}(\mathbf{r}_c)}{\mathrm{Rku}_0}\right) \times 100\% \tag{23}$$

In Table 4, we compare our predicted surface roughness data with four biological examples: trout with mucus, red maple leaf, back of human hand, flying lizard, thus obtaining the sought after material property data.

The surface skewness and kurtosis data are obtained in literature.[162] And two possible (r_1, r_2) pairs are given for positive and negative ε_2. The deviation of each case is very low. The error-iteration plot and the determinant of Jacobian matrix for the surface of *Salmo trutta* are shown in Fig. 10. By reducing the penalty parameter λ, the calculation converges faster. However, if λ is very small ($\lambda < 10^{-4}$), the calculation diverges because the Jacobian becomes singular. Fig. 10(b) shows that increasing penalty parameter can also cause a singular Jacobian.

In partial summary, we show that the inverse problem is an ill-posed problem, and we cannot guarantee a unique, stable result without introducing more information. Some of the alternatives are: (1) find the anchoring coefficients that are closest to zero; (2) compute higher-order (more than 4th-order) moment of the surface profile and conclude the unique anchoring coefficients. This method is also equivalent to method of moments in classical statistical inference.[163]

4. Conclusions

In summary, we studied the wrinkling profiles of biological and synthetic cholesteric liquid crystals driven by surface anchoring, using a generalized Rapini–Papoular model of order $2m$. We obtained the analytic solution of the surface wrinkling model under a small-wrinkling approximation, where the surface profile is a linear combination of $4m(m+1)$ distinct wrinkling modes. The direct numerical simulation validates our linearized solutions. We conducted a comprehensive examination of the surface roughness by adapting statistical approaches from hard surfaces, and we developed a curvature-based method of soft surfaces. In this paper, the surface roughness of CLC surfaces driven by anchoring is studied through evaluating the curvature, higher-order moments, autocorrelation function and autocorrelation length. The numerical simulation predicts that the average magnitude of the scaled mean curvature has a lower bound of 0.0643, achieved when the signs of three anchoring coefficients (μ_2, μ_4, μ_6) alternate. We studied the 2nd to the 4th-order moments of the surface profile, which correspond to the root mean square (Sq), skewness (Rsk), and kurtosis (Rku). The root mean square characterizes the surface deviation, and the skewness and kurtosis evaluates the bias and sharpness/peakness. We also concluded the lower bounds of both Sq and Rku in the Rapini–Papoular model. The lower bounds are achieved when the anchoring coefficients alternate sign. The autocorrelation function (acf) and autocorrelation length (Sal) distinguish a low- or a high-frequency dominated surface, and they provide a visualization of the $4m(m+1)$ distinct wrinkling modes.

Finally, we studied the inverse engineering problem. The inverse engineering problem aims to find the indirect anchoring coefficients (material property) by measuring the direct surface roughness. The significance of the inverse problem is that it reverses the difficulty of experiments, since the surface profile (the result of forward problem) is generally easier to obtain than the physics (input of the forward problem). However, the inverse problem is ill-posed, and it requires more information to provide unique and stable anchoring coefficients. Restricted by the lack of experimental data in literature, we calculated the anchoring coefficients of some biological systems by assuming they are close to zero. Our approach can be generalized to calculate r_3, r_4, ..., *etc.* if the data of higher-order moments are available.

The significance and original contributions are summarized as follow:

1. Surface wrinkling profile is a linear combination of different fundamental wrinkling modes. The **C**-matrix provides details of frequency analysis and the autocorrelation function/length demonstrates a method of visualization: Fig. 2 and 9, eqn (21).

2. We provide the analytic solution for surface wrinkling under small-wrinkling approximation. The analytic solution matches with numerical solution. The curvature distribution shows rich complexity needed for multifunctionality: Fig. 4 and 6, eqn (11).

3. A curvature-based approach $\overline{H^{*2}}$ is shown to be an proper surface roughness parameter, which also serves to quantify definitions of surface energy: Fig. 5, eqn (16).

4. Higher-order statistical moments are widely used in studying metal surface roughness, and they are shown to be suitable for soft matter surfaces in this paper: Fig. 7 and 8, eqn (17)–(19), Tables 2 and 3.

5. The inverse engineering problem provides a promising application that measures surface anchoring coefficients based on simple experiment: Fig. 10, eqn (22).

In conclusion, this paper combines theoretical and numerical insights into the study of biological and synthetic cholesteric liquid crystals surfaces. With a comprehensive understanding of the surface wrinkling profiles induced by anchoring, the theoretical framework, numerical simulations, and conclusions presented in this paper have potential applications in roughness-dominated processes and phenomena in both industry and biology.

Author contributions

ZW wrote the original draft. PS and ADR reviewed and edited the manuscript. ZW contributed to the data curation and visualization. PS and ADR contributed to the funding acquisition, supervision and project administration. ZW, PS and ADR contributed to the conceptualization, formal analysis and methodology.

Data availability

The data and derivations supporting this article have been included as part of the ESI.† The scheme implemented in this research is a standard finite difference approach. The software and data visualization tool used in this research is MatLab.

Conflicts of interest

There are no conflicts to declare.

Acknowledgements

This work was supported by the Natural Science and Engineering Research Council of Canada (NSERC) (Grant number: 223086). AR thanks McGill University for financial support through the James McGill Professor appointment. This research was enabled in part by the support provided by Calcul Québec, the BC DRI Group, and the Digital Research Alliance of Canada (**https://alliancecan.ca/alliancecan.ca**). ZW thanks the Faculty of Engineering for the MEDA scholarship program to assist his PhD study.

Notes and references

1 M. Roth, M. D'Acunzi, D. Vollmer and G. K. Auernhammer, *J. Chem. Phys.*, 2010, **132**, 124702.
2 A. D. Rey, *Rheol. Acta*, 1996, **35**, 400–409.
3 F. Giavazzi, S. Crotti, A. Speciale, F. Serra, G. Zanchetta, V. Trappe, M. Buscaglia, T. Bellini and R. Cerbino, *Soft Matter*, 2014, **10**, 3938–3949.
4 H. K. Bisoyi and Q. Li, *Acc. Chem. Res.*, 2014, **47**, 3184–3195.
5 Z.-g Zheng, Y. Li, H. K. Bisoyi, L. Wang, T. J. Bunning and Q. Li, *Nature*, 2016, **531**, 352–356.
6 I. Dierking, *Symmetry*, 2014, **6**, 444–472.
7 V. Sharma, M. Crne, J. O. Park and M. Srinivasarao, *Mater. Today: Proc.*, 2014, **1**, 161–171.
8 Y. Tang, C. Lu and R. Xiong, *ACS Nano*, 2024, **18**, 14629–14639.
9 Y. Luo, Y. Li, K. Liu, L. Li, W. Wen, S. Ding, Y. Huang, M. Liu, C. Zhou and B. Luo, *Biomacromolecules*, 2023, **24**, 2942–2954.
10 Y. Bouligand, *Tissue Cell*, 1972, **4**, 189–217.
11 Y. Bouligand, *C. R. Chim*, 2008, **11**, 281–296.
12 K. M. Lee, V. P. Tondiglia, M. Rumi and T. J. White, *J. Polym. Sci., Part B: Polym. Phys.*, 2018, **56**, 1087–1093.
13 J.-S. Hu, B.-Y. Zhang, Y.-Y. Zheng and Q.-Y. Li, *React. Funct. Polym.*, 2005, **64**, 1–11.
14 B.-Y. Zhang, J.-S. Hu, Y.-G. Jia and B.-G. Du, *Macromol. Chem. Phys.*, 2003, **204**, 2123–2129.
15 F. Kameche, W. Heni, S. Telitel, D. Ge, L. Vidal, F. Dumur, D. Gigmes, J. Lalevee, S. Marguet and L. Douillard, *et al.*, *Mater. Today*, 2020, **40**, 38–47.
16 Y. Wang, S. Wang, S. Zhang, O. A. Scherman, J. J. Baumberg, T. Ding and H. Xu, *Nano Res.*, 2018, **11**, 6384–6390.
17 Z. Liang, Y. Zhao, H. Gao, D. Wang, Z. Miao, H. Cao, Z. Yang and W. He, *Liq. Cryst.*, 2021, **48**, 2016–2026.
18 J. Liu, S. Zhang, Z. Wang, X. Xia, J. Zhang, Y. Yu, Y. Xiao, Y. Ren, J. Chen and B. Yang, *et al.*, *Nat. Commun.*, 2024, **15**, 1–11.
19 M. Mitov, *Soft Matter*, 2017, **13**, 4176–4209.
20 A. Scarangella, V. Soldan and M. Mitov, *Nat. Commun.*, 2020, **11**, 4108.
21 O. F. A. Gutierrez and A. D. Rey, *Soft Matter*, 2017, **13**, 8076–8088.
22 P. Rofouie, D. Pasini and A. D. Rey, *Colloid Interface Sci. Commun.*, 2014, **1**, 23–26.
23 M.-M. Giraud-Guille, L. Besseau and R. Martin, *J. Biomech.*, 2003, **36**, 1571–1579.
24 M. M. G. Guille, G. Mosser, C. Helary and D. Eglin, *Micron*, 2005, **36**, 602–608.
25 M. H. Chow, K. T. Yan, M. J. Bennett and J. T. Wong, *Eukaryotic Cell*, 2010, **9**, 1577–1587.
26 S. L. Ilca, X. Sun, K. El Omari, A. Kotecha, F. de Haas, F. DiMaio, J. M. Grimes, D. I. Stuart, M. M. Poranen and J. T. Huiskonen, *Nature*, 2019, **570**, 252–256.
27 J. A. Kluge, O. Rabotyagova, G. G. Leisk and D. L. Kaplan, *Trends Biotechnol.*, 2008, **26**, 244–251.
28 D. Saravanan, *et al.*, *J. Text. Apparel, Technol. Manage.*, 2006, **5**, 1–20.
29 R. Kemkemer, D. Kling, D. Kaufmann and H. Gruler, *Eur. Phys. J. E: Soft Matter Biol. Phys.*, 2000, **1**, 215–225.
30 R. Kemkemer, V. Teichgräber, S. Schrank-Kaufmann, D. Kaufmann and H. Gruler, *Eur. Phys. J. E:Soft Matter Biol. Phys.*, 2000, **3**, 101–110.
31 Y. Tan, B. Hu, J. Song, Z. Chu and W. Wu, *Nano-Micro Lett.*, 2020, **12**, 1–42.
32 P. J. Yoo and H. H. Lee, *Macromolecules*, 2005, **38**, 2820–2831.
33 X.-F. Wu, Y. A. Dzenis and K. W. Strabala, *Meccanica*, 2007, **42**, 273–282.
34 A. Cutolo, V. Pagliarulo, F. Merola, S. Coppola, P. Ferraro and M. Fraldi, *Mater. Des.*, 2020, **187**, 108314.
35 L. Jin, PhD thesis, Harvard University, 2014.
36 Q. Wang and X. Zhao, *Sci. Rep.*, 2015, **5**, 8887.

37 V. Trujillo, J. Kim and R. C. Hayward, *Soft Matter*, 2008, **4**, 564–569.
38 B. Dortdivanlioglu, N. E. D. Yilmaz, K. Goh, X. Zheng and C. Linder, *J. Elasticity*, 2021, 1–17.
39 W. Hong, X. Zhao and Z. Suo, *Appl. Phys. Lett.*, 2009, **95**, 111901.
40 D. Chen, S. Cai, Z. Suo and R. C. Hayward, *Phys. Rev. Lett.*, 2012, **109**, 038001.
41 Q. Liu, T. Ouchi, L. Jin, R. Hayward and Z. Suo, *Phys. Rev. Lett.*, 2019, **122**, 098003.
42 L. Norlén, *J. Invest. Dermatol.*, 2001, **117**, 823–829.
43 G. Perkins and T. Frey, *Micron*, 2000, **31**, 97–111.
44 F. Joubert and N. Puff, *Membranes*, 2021, **11**, 465.
45 J.-F. Mangin, D. Riviere, A. Cachia, E. Duchesnay, Y. Cointepas, D. Papadopoulos-Orfanos, P. Scifo, T. Ochiai, F. Brunelle and J. Régis, *NeuroImage*, 2004, **23**, S129–S138.
46 K. Garcia, C. Kroenke and P. Bayly, *Philos. Trans. R. Soc., B*, 2018, **373**, 20170321.
47 G. F. Striedter, S. Srinivasan and E. S. Monuki, *Annu. Rev. Neurosci.*, 2015, **38**, 291–307.
48 F. H. P. de Moraes, F. Sudo, M. Carneiro Monteiro, B. R. de Melo, P. Mattos, B. Mota and F. Tovar-Moll, *Sci. Rep.*, 2024, **14**, 3222.
49 P. Rofouie, D. Pasini and A. D. Rey, *Soft Matter*, 2015, **11**, 1127–1139.
50 P. Rofouie, D. Pasini and A. D. Rey, *Soft Matter*, 2017, **13**, 5366–5380.
51 H. Goto, *IOP Conference Series: Materials Science and Engineering*, 2014, p. 012013.
52 H. Nagai, X. Liang, Y. Nishikawa, K. Nakajima and K. Urayama, *Macromolecules*, 2016, **49**, 9561–9567.
53 Z. Wang, P. Servio and A. Rey, *Colloid Interface Sci. Commun.*, 2021, **41**, 100372.
54 Z. Wang, P. Servio and A. D. Rey, *Nanomaterials*, 2022, **12**, 1555.
55 Z. Wang, P. Servio and A. Rey, *Phys. Rev. E*, 2022, **105**, 034702.
56 A. Ryabchun and A. Bobrovsky, *Adv. Opt. Mater.*, 2018, **6**, 1800335.
57 I. Tobasco, Y. Timounay, D. Todorova, G. C. Leggat, J. D. Paulsen and E. Katifori, *Nat. Phys.*, 2022, **18**, 1099–1104.
58 T. Wen, T. Ma, J. Qian, Z. Song, X. Jiang and Y. Yao, *Nat. Commun.*, 2024, **15**, 10821.
59 Z. Wang, P. Rofouie and A. D. Rey, *Crystals*, 2019, **9**, 190.
60 Z. Wang, P. Servio and A. D. Rey, *Phys. Rev. E*, 2020, **101**, 062705.
61 Z. Wang, P. Servio and A. D. Rey, *Front. Soft Matter*, 2022, **2**, 904069.
62 Z. Wang, P. Servio and A. D. Rey, *Soft Matter*, 2023, **19**, 9344.
63 Z. Wang, P. Servio and A. D. Rey, *Front. Soft Matter*, 2023, **3**, 1123324.
64 A.-G. Cheong, A. D. Rey and P. T. Mather, *Phys. Rev. E: Stat., Nonlinear, Soft Matter Phys.*, 2001, **64**, 041701.
65 A.-G. Cheong and A. D. Rey, *J. Chem. Phys.*, 2002, **117**, 5062–5071.
66 A.-G. Cheong and A. D. Rey, *Phys. Rev. E: Stat., Nonlinear, Soft Matter Phys.*, 2002, **66**, 021704.
67 A.-G. Cheong and A. D. Rey, *Continuum Mech. Thermodyn.*, 2002, **14**, 263–279.
68 A.-G. Cheong and A. D. Rey, *Liq. Cryst.*, 2004, **31**, 1271–1284.
69 S. Schauer, M. Worgull and H. Hölscher, *Soft Matter*, 2017, **13**, 4328–4334.
70 Y. Nakamura and Y. Tomonari, *J. Fluid Mech.*, 1982, **123**, 363–378.
71 F. Farshad, H. Rieke and J. Garber, *J. Pet. Sci. Eng.*, 2001, **29**, 139–150.
72 G. Severino, *J. Fluid Mech.*, 2024, **1000**, R1.
73 W.-K. Hong, S. Song, D.-K. Hwang, S.-S. Kwon, G. Jo, S.-J. Park and T. Lee, *Appl. Surf. Sci.*, 2008, **254**, 7559–7564.
74 G. Palasantzas, J. T. M. De Hosson and J. Barnas, *Surf. Sci.*, 2002, **507**, 541–545.
75 A. Larena, F. Millán, G. Pérez and G. Pinto, *Appl. Surf. Sci.*, 2002, **187**, 339–346.
76 A. Trügler, J.-C. Tinguely, J. R. Krenn, A. Hohenau and U. Hohenester, *Phys. Rev. B: Condens. Matter Mater. Phys.*, 2011, **83**, 081412.
77 K. Kubiak, M. Wilson, T. Mathia and P. Carval, *Wear*, 2011, **271**, 523–528.
78 A. AlRatrout, M. J. Blunt and B. Bijeljic, *Proc. Natl. Acad. Sci. U. S. A.*, 2018, **115**, 8901–8906.
79 B. N. Persson, O. Albohr, U. Tartaglino, A. I. Volokitin and E. Tosatti, *J. Phys.: Condens. Matter*, 2004, **17**, R1.
80 F. Svahn, Å. Kassman-Rudolphi and E. Wallén, *Wear*, 2003, **254**, 1092–1098.
81 J. Koo and C. Kleinstreuer, *Int. J. Heat Mass Transfer*, 2005, **48**, 2625–2634.
82 A. Toloei, V. Stoilov and D. Northwood, *ASME International mechanical engineering congress and exposition*, 2013, p. V02BT02A054.
83 C. Hagen, A. Hognestad, O. Ø. Knudsen and K. Sørby, *Prog. Org. Coat.*, 2019, **130**, 17–23.
84 K. Singh, N. Paliwal and K. Kasamias, *Sci. Rep.*, 2024, **14**, 1785.
85 A. Gujrati, S. R. Khanal, L. Pastewka and T. D. Jacobs, *ACS Appl. Mater. Interfaces*, 2018, **10**, 29169–29178.
86 I. J. Cartwright and J. A. Higgins, *J. Biol. Chem.*, 2001, **276**, 48048–48057.
87 S. R. Wilkinson, M. C. Taylor, S. Touitha, I. L. Mauricio, D. J. Meyer and J. M. Kelly, *Biochem. J.*, 2002, **364**, 787–794.
88 H. F. Lodish, N. Kong, M. Snider and G. J. Strous, *Nature*, 1983, **304**, 80–83.
89 E. C. Mandon, S. F. Trueman and R. Gilmore, *Cold Spring Harbor Perspect. Biol.*, 2013, **5**, a013342.
90 E. Kuwert and R. Schätzle, *J. Differ. Geom.*, 2001, **57**, 409–441.
91 E. Aulisa, A. Gruber and M. Toda, *Geom., Integrability Quantization, Papers Lecture Ser.*, 2024, **29**, 1–10.
92 M. Toda and B. Athukoralage, *AIP Conference Proceedings*, 2013, pp. 883–886.
93 O.-Y. Zhong-Can and W. Helfrich, *Phys. Rev. A: At., Mol., Opt. Phys.*, 1989, **39**, 5280.

94 F. Campelo, C. Arnarez, S. J. Marrink and M. M. Kozlov, *Adv. Colloid Interface Sci.*, 2014, **208**, 25–33.
95 W. Helfrich, *Giant Vesicles*, 1999, 51–70.
96 W. Bao and Y. Li, *SIAM J. Numerical Anal.*, 2025, **63**, 103–121.
97 G. Dziuk, *Numer. Math.*, 2008, **111**, 55–80.
98 S. R. Brown, *Geophys. Res. Lett.*, 1987, **14**, 1095–1098.
99 S. R. Nayak, J. Mishra and G. Palai, *Image Vision Comput.*, 2019, **89**, 21–34.
100 A. Majumdar and B. Bhushan, *J. Tribol.*, 1990, **112**, 205–216.
101 A. D. Rey, *Langmuir*, 2001, **17**, 1922–1927.
102 D. Schlegel, M. Folea, A. Roman and P. Nardin, *Rec. Res. Manuf. Eng.*, 2011, 152–155.
103 A. W. Hashmi, H. S. Mali, A. Meena, M. F. Hashmi and N. D. Bokde, *Comput. Model. Eng. Sci.*, 2023, **135**, 917–1005.
104 C. T. Collier, E. Hesse, L. Taylor, Z. Ulanowski, A. Penttilä and T. Nousiainen, *J. Quant. Spectrosc. Radiat. Transfer*, 2016, **182**, 225–239.
105 C. Tay, S. Wang, C. Quan and H. Shang, *Opt. Commun.*, 2003, **218**, 1–10.
106 S. Banerjee, R. Yang, C. E. Courchene and T. E. Conners, *Ind. Eng. Chem. Res.*, 2009, **48**, 4322–4325.
107 S. Lawes, S. Hainsworth, P. Blake, K. Ryder and A. Abbott, *Tribol. Lett.*, 2010, **37**, 103–110.
108 S. Al-Jeshi and A. Neville, *Desalination*, 2006, **189**, 221–228.
109 N. Almqvist, *Surf. Sci.*, 1996, **355**, 221–228.
110 C.-L. Tien, H.-M. Yang and M.-C. Liu, *Thin Solid Films*, 2009, **517**, 5110–5115.
111 V. Niola, G. Nasti and G. Quaremba, *J. Mater. Process. Technol.*, 2005, **164**, 1410–1415.
112 U. Kühnau, A. Petrov, G. Klose and H. Schmiedel, *Phys. Rev. E: Stat. Phys., Plasmas, Fluids, Relat. Interdiscip. Top.*, 1999, **59**, 578.
113 D.-F. Gu, S. Uran and C. Rosenblatt, *Liq. Cryst.*, 1995, **19**, 427–431.
114 Y. Choi, H. Yokoyama and J. S. Gwag, *Opt. Express*, 2013, **21**, 12135–12144.
115 A. Marino, V. Tkachenko, E. Santamato, N. Bennis, X. Quintana, J. Otón and G. Abbate, *J. Appl. Phys.*, 2010, **107**, 073109.
116 A. D. Rey, *Mol. Cryst. Liq. Cryst. Sci. Technol., Sect. A*, 2001, **369**, 63–74.
117 A. D. Rey, *Macromol. Theory Simul.*, 2004, **13**, 686–696.
118 A. D. Rey, *Soft Matter*, 2007, **3**, 1349–1368.
119 A. D. Rey, *J. Chem. Phys.*, 2004, **120**, 2010–2019.
120 A. D. Rey, *Rheol. Acta*, 2000, **39**, 13–19.
121 A. D. Rey, *Phys. Rev. E: Stat. Phys., Plasmas, Fluids, Relat. Interdiscip. Top.*, 2000, **61**, 1540.
122 A. D. Rey, *Macromol. Theory Simul.*, 2000, **9**, 156–165.
123 A. D. Rey, E. Herrera-Valencia and Y. K. Murugesan, *Liq. Cryst.*, 2014, **41**, 430–451.
124 Y. K. Murugesan and A. D. Rey, *J. Non-Newtonian Fluid Mech.*, 2010, **165**, 32–44.
125 A. D. Rey, *J. Non-Newtonian Fluid Mech.*, 2001, **96**, 45–62.
126 D. V. Shmeliova, S. V. Pasechnik, S. S. Kharlamov, A. V. Zakharov, E. P. Pozhidaev, V. A. Barbashov and T. P. Tkachenko, *Crystals*, 2020, **10**, 1029.
127 D. V. Shmeliova, S. V. Pasechnik, S. S. Kharlamov, A. V. Dubtsov, A. V. Zakharov, S. Loebner and S. Santer, *Symmetry*, 2023, **15**, 722.
128 A. V. Zakharov, *Phys. Solid State*, 2018, **60**, 610–615.
129 J. Zhao, X. Yang, Y. Gong and Q. Wang, *Comput. Methods Appl. Mech. Eng.*, 2017, **318**, 803–825.
130 R. J. Fox, W.-R. Chen, C. Do, S. J. Picken, M. G. Forest and T. J. Dingemans, *Rheol. Acta*, 2020, **59**, 727–743.
131 M. G. Forest, Q. Wang and R. Zhou, *Soft Matter*, 2013, **9**, 5207–5222.
132 D. Chillingworth, M. G. Forest, R. Lauterbach and C. Wulff, *Arch. Ration. Mech. Anal.*, 2021, **242**, 1229–1287.
133 A. D. Rey, *J. Chem. Phys.*, 1999, **110**, 9769–9770.
134 A. D. Rey, *Liq. Cryst.*, 1999, **26**, 913–917.
135 A. D. Rey, *Phys. Rev. E: Stat. Phys., Plasmas, Fluids, Relat. Interdiscip. Top.*, 1999, **60**, 1077.
136 P. Yue, J. J. Feng, C. Liu and J. Shen, *J. Colloid Interface Sci.*, 2005, **290**, 281–288.
137 F. H. Lin and C. Liu, *J. Partial Differ. Equ.*, 2001, **14**, 289–330.
138 C. Liu and H. Sun, *Discrete Continuous Dyn. Syst.*, 2008, **23**, 455–475.
139 C. Liu and N. J. Walkington, *SIAM J. Numerical Anal.*, 2000, **37**, 725–741.
140 A. D. Rey, *Phys. Rev. E: Stat., Nonlinear, Soft Matter Phys.*, 2005, **72**, 011706.
141 W. Jiang and Q. Zhao, *Phys. D*, 2019, **390**, 69–83.
142 J. Cahn and D. Hoffman, *Acta Metall.*, 1974, **22**, 1205–1214.
143 D. W. Hoffman and J. W. Cahn, *Surf. Sci.*, 1972, **31**, 368–388.
144 A.-G. Cheong and A. D. Rey, *J. Chem. Phys.*, 2002, **117**, 5062–5071.
145 O. F. A. Gutierrez and A. D. Rey, *Soft Matter*, 2018, **14**, 1465–1473.
146 Z. Wang, P. Servio and A. D. Rey, *Entropy*, 2020, **22**, 909.
147 D. U. Zamora Cisneros, Z. Wang, N.-M. Dorval Courchesne, M. J. Harrington and A. D. Rey, *Front. Soft Matter*, 2024, **4**, 1359128.
148 S. Givli, H. Giang and K. Bhattacharya, *SIAM J. Appl. Math.*, 2012, **72**, 489–511.
149 A. Agrawal, *Biomech. Model. Mechanobiol.*, 2025, 1–5.
150 Z. Tu and Z. Ou-Yang, *J. Phys. A: Math. Gen.*, 2004, **37**, 11407.
151 P. Podulka, *Coatings*, 2022, **13**, 74.
152 A. Francisco and N. Brunetière, *Proc. Inst. Mech. Eng., Part J*, 2016, **230**, 747–768.
153 P. Podulka, W. Macek, B. Zima, G. Lesiuk, R. Branco and G. Królczyk, *Measurement*, 2023, **222**, 113640.
154 R. Dusséaux and E. Vannier, *Biosyst. Eng.*, 2022, **220**, 87–102.
155 C. T. Kelley and D. E. Keyes, *SIAM J. Numerical Anal.*, 1998, **35**, 508–523.
156 X.-l Luo, *Appl. Math. Comput.*, 2010, **216**, 1752–1762.
157 D. Hüser, J. Hüser, S. Rief, J. Seewig and P. Thomsen-Schmidt, *Meas. Sci. Technol.*, 2016, **27**, 085005.
158 A. Busse and T. Jelly, *J. Turbulence*, 2023, **24**, 57–81.

159 D. J. Whitehouse, *Handbook of surface and nanometrology*, Taylor & Francis, 2002.
160 K. Pearson, *Philos. Trans. R. Soc., A*, 1916, **216**, 429–457.
161 S. Panda, A. Panzade, M. Sarangi and S. Roy Chowdhury, *J. Tribol.*, 2017, **139**, 031402.
162 D. K. Wainwright, G. V. Lauder and J. C. Weaver, *Methods Ecol. Evolution*, 2017, **8**, 1626–1638.
163 L. Wasserman, *All of statistics: a concise course in statistical inference*, Springer Science & Business Media, 2013.

